

Chapter 2

Probing the Structure and Assembly of Nearby Field Spirals

Abstract We use the bulge Sérsic index n and bulge-to-total ratio (B/T) to explore the fundamental question of how bulges form. We perform 2D bulge-disk-bar decomposition on H -band images of 143 bright, high mass ($M_* \geq 1.0 \times 10^{10} M_\odot$) low-to-moderately inclined ($i < 70^\circ$) spirals. Our results are: (1) Our H -band bar fraction ($\sim 58\%$) is consistent with that from ellipse fits. (2) 70 % of the stellar mass is in disks, 10% in bars, and 20% in bulges. (3) *A large fraction ($\sim 69\%$) of bright spirals have $B/T \leq 0.2$, and $\sim 76\%$ have low $n \leq 2$ bulges. These bulges exist in barred and unbarred galaxies across a wide range of Hubble types.* (4) About 65% (68%) of bright spirals with $n \leq 2$ ($B/T \leq 0.2$) bulges host bars, suggesting a possible link between bars and bulges. (5) We compare the results with predictions from a set of Λ CDM models. In the models, a high mass spiral can have a bulge with a present-day low $B/T \leq 0.2$ only if it did not undergo a major merger since $z \leq 2$. The predicted fraction ($\sim 1.6\%$) of high mass spirals, which have undergone a major merger since $z \leq 4$ and host a bulge with a present-day low $B/T \leq 0.2$, is *a factor of over thirty smaller* than the observed fraction ($\sim 66\%$) of high mass spirals with $B/T \leq 0.2$. Thus, *contrary to common perception, bulges built via major mergers since $z \leq 4$ seriously fail to account for the bulges present in $\sim 66\%$ of high mass spirals.* Most of these present-day low $B/T \leq 0.2$ bulges are likely to have been built by a combination of minor mergers and/or secular processes since $z \leq 4$.

This chapter has been previously published as Weinzirl, T., Jogee, S., Khochfar, S., Burkert, A., & Kormendy, J.: *Astrophys. J.* **696**, 411 (2009).

2.1 Introduction

The formation of galaxies is a classic problem in astrophysics. Contemporary galaxy formation models combine the well-established Λ Cold Dark Matter (Λ CDM) cosmology, which describes behavior of dark matter on very large scales, with baryonic physics to model galaxy formation. In the early Universe, pockets of dark matter decoupled from the Hubble flow, collapsed into virialized halos, and then clustered hierarchically into larger structures. Meanwhile, gas aggregated in the interiors of the halos to form rotating disks, which are the building blocks of galaxies (Steinmetz and Navarro 2002; Cole et al. 2000). Such disks are typically destroyed during major mergers of galaxies with mass ratio $M_1/M_2 > 1/4$ (e.g., Steinmetz and Navarro 2002; Naab and Burkert 2003; Burkert and Naab 2004; Mihos and Hernquist 1996). When the mass ratio is close to unity, the remnant is a spheroid with properties close to that of a classical bulge, namely a steep de Vaucouleurs $r^{1/4}$ surface brightness profile and a high ratio of ordered-to-random motion (v/σ). We shall return to this point in Sect. 2.5. Within this hierarchical framework, the disk of spiral galaxies forms when gas of higher specific angular momentum subsequently accretes around the bulge (Steinmetz and Navarro 2002; Burkert and Naab 2004).

Λ CDM-based simulations of galaxy formation face several challenges. One issue is the angular momentum problem; simulated galaxy disks have smaller scalelengths and, therefore, less specific angular momentum than their counterparts in nature (Navarro and Steinmetz 2000; Burkert and D’Onghia 2004; D’Onghia et al. 2006). A second issue is the problem of bulgeless or low bulge-to-total mass ratio (B/T) spirals. Within the Λ CDM paradigm, galaxies that had a past major merger at a time when its mass was a fairly large fraction of its present-day mass are expected to have a significant bulge with large B/T and high Sérsic index. Depending on the merger history and hence the fraction of spiral galaxies that fulfill this criterion (see Sect. 2.5.8) we can end up with a small or large fraction of present-day galaxies with low B/T .

There is rising evidence that low B/T and bulgeless galaxies are quite common in the local Universe, especially in low mass or late-type galaxies. Late-type Sd galaxies often harbor no bulge (Böker et al. 2002). Kautsch et al. (2006) and Barazza et al. (2007, 2008) also find from the analysis of several thousand late-type SDSS galaxies that 15–20% of such disk galaxies out to $z \sim 0.03$ appear bulgeless. Of the 19 local galaxies ($D < 8$ Mpc) with circular velocity $V_c > 150 \text{ km s}^{-1}$, 11 (58%) have pseudobulges instead of merger-built classical bulges (Kormendy and Fisher 2008).

Theoretical work by Koda et al. (2009) conclude the survival of disk-dominated systems in a Λ CDM universe is compatible with observational constraints provided classical bulges form only in mergers where $M_1/M_2 > 0.3$ and the primary halo has virial velocity $V_{vir} > 55 \text{ km s}^{-1}$.

Evidence also suggests that bulges with low B/T and low Sérsic index n may be common even in high mass and/or early-type spirals. Balcells et al. (2003) report that early-type disk galaxies tend to have $n < 3$ and often from 1 to 2.

Laurikainen et al. (2007) find barred and unbarred early-type disk galaxies to have mean B/T between 0.25 and 0.35, while later Hubble types have $B/T < 0.2$; they also find mean bulge Sérsic indices to be ~ 2.5 or less across the Hubble sequence. Graham and Worley (2008) report low B/D ratios across the Hubble sequence based on bulge-disk decomposition of K -band images of local spiral galaxies. They suggest that these low values are problematic for Λ CDM simulations, but no quantitative assessment of the extent of the problems is presented.

These emerging statistics on the fraction of bulgeless ($B/T \sim 0$) galaxies, and galaxies with low B/T and low n bulges provide important first constraints. More work is needed to fully explore the distribution of bulge properties in both high and low mass galaxies. In particular, we need to explore how the observed distributions of bulge B/T and n compare with the predictions from Λ CDM-based simulations of galaxy evolution. To the best of our knowledge, few such quantitative comparisons have been attempted, so that it remains unclear how serious the problem of low B/T galaxies is. This study is an attempt to derive robust observational constraints on bulge properties in high mass spirals and to attempt such a comparison with models.

Completely resolving the issue of low B/T systems will require understanding the different types of bulges and their formation pathways. Bulges are commonly divided in several groups: classical bulges, boxy/peanut bulges, and ‘pseudobulges’ or disky bulges. Classical bulges are believed to be built by major mergers ($M_1/M_2 \geq 1/4$) and the associated violent relaxation of stars. They are associated with modest-to-high bulge Sérsic indices, in the range $2 < n < 6$ (Hopkins et al. 2009a; Springel et al. 2005; Robertson et al. 2006, Sect. 2.5.8). Boxy/peanut bulges are believed to be the result of vertical resonances and buckling instabilities in bars, which are viewed at high inclination (Combes and Sanders 1981; Combes et al. 1990; Pfenniger and Norman 1990; Bureau and Athanassoula 2005; Athanassoula 2005; Martinez-Valpuesta et al. 2006). Pseudobulges or disky bulges are believed to form as a result of gas inflow into the central kiloparsec and subsequent star formation building a compact disky, high v/σ stellar component (Kormendy 1993; Jogee et al. 1999; Kormendy and Kennicutt 2004, hereafter KK04; Jogee et al. 2005, Athanassoula 2005; Kormendy and Fisher 2005).

Pseudobulges tend to have a bulge $n < 2.5$ (Kormendy and Fisher 2005; Fisher and Drory 2008).

One possibility for the formation of disky bulges or pseudobulges is the idea of secular evolution (Kormendy 1993; KK04; Jogee et al. 2005), where a stellar bar or globally oval structure in a *non-interacting* galaxy drives the gas inflow into the inner kpc via shocks and gravitational torque. Another idea for building disky bulges is that the gas inflow into the inner kiloparsec is driven by *external non-secular processes*, such as tidal interaction and minor mergers. The gas inflow in such cases can be caused by a tidally induced non-axisymmetric feature, such as a bar (e.g., Quinn et al. 1993; Hernquist and Mihos 1995), and by tidal torques from the companion. The subsequent central star formation can still form a compact high v/σ stellar component, *aka* a pseudobulge.

Throughout this paper, we avoid making any *a priori* assumptions about the origin of different types of bulges by simply referring to them according to their bulge Sérsic index n or bulge-to-total mass ratio (B/T). We consider bulges of high ($n \geq 4$), intermediate ($2 < n < 4$) and low ($n \leq 2$) index, as well as those of low or high B/T .

The structural properties of galaxy components, such as bulges, disks, and bars can be derived through the decomposition of the 2D light distribution, taking into account the PSF. Many early studies have performed only two component 2D bulge-disk decomposition (e.g., Allen et al. 2006; Byun and Freeman 1995; de Jong 1996; Simard et al. 1998; Wadadekar et al. 1999), ignoring the contribution of the bar, even in strongly barred galaxies. However, recent work has shown that it is important to include the bar in 2D decomposition of barred galaxies, else the B/T ratio can be artificially inflated, and bulge properties skewed (e.g., Laurikainen et al. 2005, 2007). Furthermore, since most ($\geq 60\%$) bright spiral galaxies are barred in the NIR (Eskridge et al. 2000; Laurikainen et al. 2004; Marinova and Jogee 2007, hereafter MJ07; Menéndez-Delmestre et al. 2007), the inclusion of the bar is quite important. This has led to several recent studies, where 2D bulge-disk-bar decomposition are being performed (e.g., Laurikainen et al. 2007; Reese et al. 2007; Gadotti and Kauffmann 2007).

Another advantage of bulge-disk-bar decomposition over bulge-disk decomposition is that the former allows us to constrain the properties of the bar itself. Bars provide the most important internal mechanism for redistributing angular momentum in baryonic and dark matter components (e.g., Weinberg 1985; Debattista and Sellwood 1998, 2000; Athanassoula 2002; Berentzen et al. 2006). They efficiently drive gas inflows into the central kpc, feed central starbursts (Elmegreen 1994; Knapen et al. 1995; Hunt and Malkan 1999; Jogee et al. 1999; Jogee et al. 2005; Jogee 2006) and lead to the formation of disky or pseudobulges (see above). Furthermore, the prominence of strong bars out to $z \sim 1$ over the last 8 Gyr (Jogee et al. 2004; Sheth et al. 2008) suggest that bars have been present over cosmological times and can shape the dynamical and secular evolution of disks. Thus, quantifying bar properties, such as the fractional light and mass ratio (Bar/T), can yield insight into these processes.

In this paper, we constrain the properties of bulges and bars along the Hubble sequence, and compare our results with Λ CDM-based simulations of galaxy evolution. In Sect. 2.2, we define our complete sample of 143 bright ($M_B \leq -19.3$) low-to-moderately inclined ($i \leq 70^\circ$) spirals from the Ohio State University Bright Spiral Galaxy Survey (OSUBSGS; Eskridge et al. 2002), which is widely used as the local reference sample for bright spirals by numerous studies (e.g., Eskridge et al. 2000; Block et al. 2002; Buta et al. 2005; MJ07; Laurikainen et al. 2004, 2007). In Sect. 2.3, we perform 2D bulge-disk and bulge-disk-bar decompositions of H -band images using GALFIT (Peng et al. 2002), and derive fractional light ratios (B/T , Bar/T , Disk/T), as well as Sérsic indices and half light radii or scale lengths. Tests to verify the robustness of our decompositions are presented in Sect. 2.4. In Sect. 2.5, we present our results. Specifically, the total stellar mass present in bulges, disks, and bars is calculated (Sect. 2.5.2). In Sect. 2.5.3, the distribution of bulge Sérsic

index n and B/T as a function of galaxy Hubble type and stellar mass is presented, and the surprising prevalence of bulges with low Sérsic index n and low B/T is established. A comparison with other works is presented in Sect. 2.5.4. We examine how Bar/ T and bar fraction (the fraction barred disks) change as a function of host galaxy properties in Sect. 2.5.5. In Sect. 2.5.8, we compare our observed distribution of bulge B/T and n in high mass ($M_\star \geq 1.0 \times 10^{10} M_\odot$) spirals with predictions from Λ CDM cosmological semi-analytical models. Section 2.6 summarizes our results.

2.2 Sample Properties

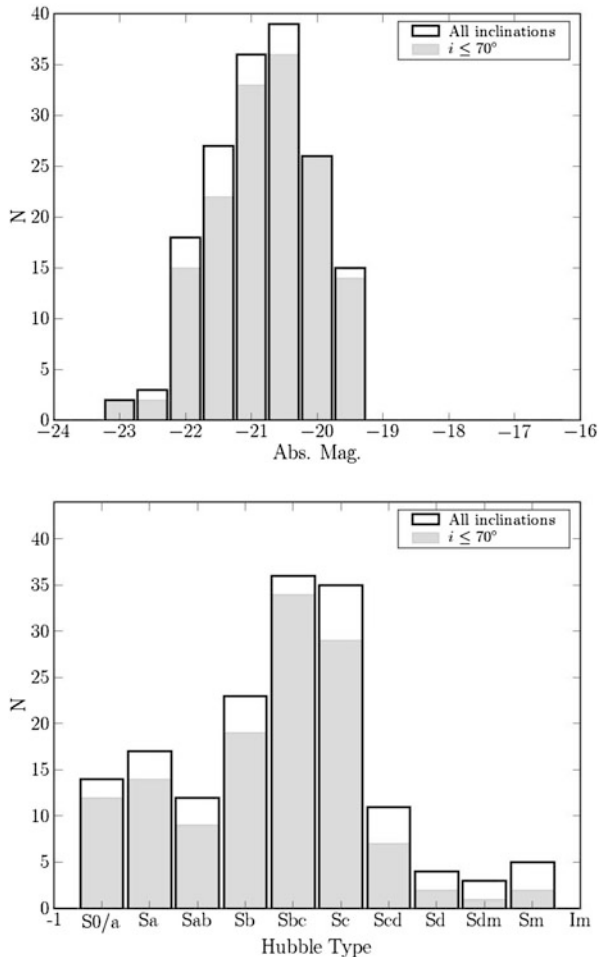
2.2.1 OSUBSGS

Our dataset is derived from the 182 H -band images from the public data release of the Ohio State University Bright Spiral Galaxy Survey (OSUBSGS; Eskridge et al. 2002). These galaxies are a subset of the RC3 catalog that have $m_B \leq 12$, Hubble types $0 \leq T \leq 9$ (S0/a to Sm), $D_{25} \leq 6'.5$, and $-80^\circ < \delta < +50^\circ$. Imaging of OSUBSGS galaxies spans optical and near infrared (NIR) wavelengths with $BVRJHK$ images available for most galaxies. OSUBSGS images were acquired on a wide range of telescopes with apertures ranging from 0.9–2.4 m. The JHK data were acquired with a variety of telescopes and detectors, but mainly with the 1.8 m Perkins reflector at Lowell Observatory and the CTIO 1.5 m telescope with the OSIRIS detector, having 18.5 micron pixels (Depoy et al. 1993). Pixel scale is dependent on the telescope and for these observations ranged between 1 and $1.50''/\text{pix}$. Exposure times were heterogeneous, but the total observing time per object was typically between 10 and 15 min in H . The resulting limiting H -band surface brightness is $\sim 20 \text{ mag arcsec}^{-2}$. The typical limiting surface brightnesses of the images $\sim 26 \text{ mag arcsec}^{-2}$ in B -band and $\sim 20 \text{ mag arcsec}^{-2}$ in H -band (Eskridge et al. 2002). The seeing depends on observing time and location. We find the H -band images have seeing of $\sim 3''$.

We choose to use the NIR images rather than optical ones for several reasons. Firstly, NIR images are better tracers of the stellar mass than optical images, and the mass-to-light ratio is less affected by age or dust gradients. Secondly, obscuration by dust and SF are minimized in the NIR, compared with the optical. As the K -band images are of poor quality, we settle on using the H -band images.

The OSUBSGS is widely used as the local reference sample for bright spirals by numerous studies (e.g., Eskridge et al. 2000; Böker et al. 2002; Buta et al. 2005; MJ07; Laurikainen et al. 2004, 2007). Thus, there are numerous complementary results that we can use or compare with. In particular, MJ07 have identified bars in this sample using quantitative criteria based on ellipse fitting, and characterized their sizes, position angles, and ellipticities.

Fig. 2.1 Our final sample S1 consists of 143 bright ($M_B \leq -19.3$) low-to-moderately inclined ($i \leq 70^\circ$) spirals in the OSUBSGS survey. The distribution of absolute B -band magnitude for the sample of bright spirals in the OSUBSGS survey is shown in the *top panel* before (*solid line*) and after (*shaded greyscale*) the cut to remove highly inclined ($i > 70^\circ$) spirals. The distribution of Hubble types for the sample is shown in the *bottom panel* before (*solid line*) and after (*shaded greyscale*) the cut to remove highly inclined ($i > 70^\circ$) spirals



OSUBSGS is a magnitude-limited survey with objects whose distances range up to ~ 60 Mpc. Faint galaxies are inevitably missed at larger distances, resulting in the absolute magnitude distribution in Fig. 2.1. We compare the B -band LF of this sample with a Schechter (Schechter 1976) LF (SLF) with $\Phi^* = 5.488 \times 10^{-3} \text{ Mpc}^{-3}$, $\alpha = -1.07$, and $M_B^* = -20.5$ (Efsthathiou et al. 1988) in Fig. 2.2. The volume used to determine the number density in each magnitude bin is

$$V_{max} = \frac{4\pi}{3} d_{max}^3(M), \quad (2.1)$$

where

$$d_{max}(M) = 10^{1+0.2(m_c-M)} \quad (2.2)$$

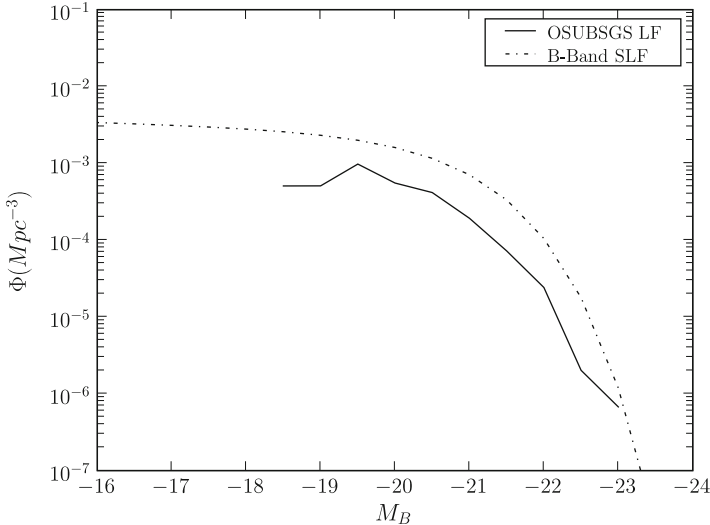


Fig. 2.2 The luminosity function of the full OSUBSGS sample is compared with the B -band Schechter luminosity function (SLF). The former is calculated as described in Sect. 2.2.1 using Eq. (2.1). The parameters for the SLF are $\Phi^* = 5.488 \times 10^{-3} \text{ Mpc}^{-3}$, $\alpha = -1.07$, and $M_B^* = -20.5$ (Efsthathiou et al. 1988), corresponding to $H_0 = 70 \text{ km s}^{-1} \text{ Mpc}^{-1}$

is the maximum distance out to which a galaxy of absolute magnitude M can be observed given the cutoff magnitude m_c . If the SLF is representative of the true LF, then Fig. 2.2 suggests that the OSUBSGS sample is seriously incomplete at $M_B > -19.3$, while at the brighter end (-19.3 to -23) the shape of its LF matches fairly well the SLF. We thus conclude that the sample is reasonably complete for bright ($M_B \leq -19.3$ or $L_B > 0.33 L^*$) galaxies.

We exclude highly inclined ($i > 70^\circ$) galaxies for which structural decomposition does not yield accurate results. Thus, our final sample S1 consists of 143 bright ($M_B \leq -19.3$) low-to-moderately inclined ($i \leq 70^\circ$) spirals with Hubble types mainly in the range S0/a to Sc (Fig. 2.1). Of the 126 for which we could derive stellar masses (see Sect. 2.2.2, most have stellar masses $M_* \geq 1.0 \times 10^{10} M_\odot$ (Fig. 2.3). Table 2.1 summarizes the morphologies, luminosities, and stellar masses of the sample. Note that there are few galaxies of late Hubble types (Scd or later) and we do not draw any conclusions on such systems from our study. In a future paper, we will tackle galaxies of lower mass and later Hubble types.

2.2.2 Stellar Masses

We derive global stellar masses for most of the OSUBSGS sample galaxies using the relation between stellar mass and rest-frame $B - V$ color from Bell et al. (2003).

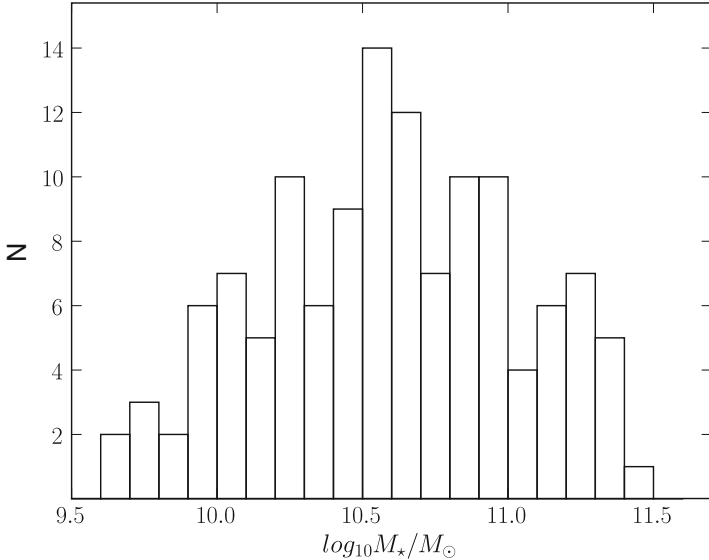


Fig. 2.3 Out of our final sample S1 of 143 bright ($M_B \leq -19.3$) low-to-moderately inclined ($i \leq 70^\circ$) OSUBSGS spirals, stellar masses could be estimated for 126 galaxies. Their stellar mass distribution is shown, as determined in Sect. 2.2.2. Most have stellar masses $M_* \geq 1.0 \times 10^{10} M_\odot$. This sample of 126 galaxies is referenced henceforth as the sample S2

Using population synthesis models, the latter study calculates stellar M/L ratio as a function of color using functions of the form $\log_{10}(M/L) = a_\lambda + b_\lambda \times Color + C$, where a_λ and b_λ are bandpass dependent constants and C is a constant that depends on the stellar initial mass function (IMF). For the V band Bell et al. (2003) find $a_\lambda = -0.628$ and $b_\lambda = 1.305$; assuming a Kroupa et al. (1993) IMF, they find $C = -0.10$. This yields an expression for the stellar mass in M_\odot for a given $B - V$ color:

$$M_* = v_{lum} 10^{-0.628 + 1.305(B-V) - 0.10}, \quad (2.3)$$

where

$$v_{lum} = 10^{-0.4(V-4.82)}. \quad (2.4)$$

Here, v_{lum} is the luminosity parametrized in terms of absolute V magnitude.

How reliable are stellar masses determined from this procedure? Clearly, the above relationship between M_* and $B - V$ cannot apply to all galaxies, and must depend on the assumed stellar IMF, and range of ages, dust, and metallicity. However, it is encouraging to note that several studies (Bell et al. 2003; Drory et al. 2004; Salucci et al. 2008) find generally good agreement between masses based on broad-band colors and those from spectroscopic (e.g., Kauffmann et al. 2003) and

Table 2.1 Sample S1 of bright ($M_B \leq -19.3$) low-to-moderately inclined ($i \leq 70^\circ$) spirals in OSUBSGS ($N = 143$)

Galaxy name (1)	Best fit (2)	Hubble type (RC3) (3)	Bar type (RC3) (4)	D (Mpc) (5)	M_B (mag) (6)	$B - V$ (mag) (7)	M_* (M_\odot) (8)
ESO138-10	PSF+ Bulge+ Disk	SA(s)cd	A	15.75	-20.2	-	-
IC0239	PSF+ Bulge+ Disk+ Bar	SAB(rs)cd	AB	15.21	-19.3	0.70	1.34e+10
IC4444	Bulge+ Disk	SAB(rs)bc	AB	28.82	-20.9	0.64	4.35e+10
IC5325	PSF+ Bulge+ Disk	SAB(rs)bc	AB	19.39	-19.6	0.56	9.78e+09
NGC0150	PSF+ Bulge+ Disk+ Bar	SB(rs)bc	B	20.57	-20.1	0.64	2.17e+10
NGC0157	PSF+ Bulge+ Disk	SAB(rs)bc	AB	22.39	-21.4	0.59	5.81e+10
NGC0210	Bulge+ Disk+ Bar	SAB(s)b	AB	21.75	-20.4	0.71	3.77e+10
NGC0278	PSF+ Bulge+ Disk	SAB(rs)b	AB	12.64	-19.5	0.64	1.24e+10
NGC0289	PSF+ Bulge+ Disk+ Bar	SAB(rs)bc	AB	20.79	-20.2	0.73	3.33e+10
NGC0428	PSF+ Bulge+ Disk+ Bar	SAB(s)m	AB	15.96	-19.4	0.44	5.28e+09
NGC0488	PSF+ Bulge+ Disk	SA(r)b	A	31.39	-21.8	0.87	2.44e+11
NGC0578	PSF+ Bulge+ Disk+ Bar	SAB(rs)c	AB	20.89	-20.5	0.51	1.87e+10
NGC0613	PSF+ Bulge+ Disk+ Bar	SB(rs)bc	B	18.75	-20.8	0.68	4.92e+10
NGC0685	Bar+ Disk	SAB(r)c	AB	16.29	-19.4	0.46	5.47e+09
NGC0779	Bulge+ Disk+ Bar	SAB(r)b	AB	18.54	-20.0	0.79	3.64e+10
NGC0864	PSF+ Bulge+ Disk+ Bar	SAB(rs)c	AB	21.43	-20.6	0.55	2.31e+10
NGC0908	PSF+ Bulge+ Disk	SA(s)c	A	19.07	-21.3	0.65	6.60e+10
NGC1042	PSF+ Bulge+ Disk	SAB(rs)cd	AB	17.89	-20.2	0.54	1.63e+10
NGC1073	PSF+ Bulge+ Disk+ Bar	SB(rs)c	B	16.29	-19.9	0.50	1.04e+10
NGC1084	PSF+ Bulge+ Disk	SA(s)c	A	18.32	-20.6	0.58	2.64e+10
NGC1087	Bar+ Disk	SAB(rs)c	AB	20.36	-20.6	0.52	2.09e+10
NGC1187	PSF+ Bulge+ Disk+ Bar	SB(r)c	B	17.46	-20.2	0.56	1.66e+10
NGC1241	PSF+ Bulge+ Disk+ Bar	SB(rs)b	B	28.50	-21.7	0.85	2.05e+11
NGC1300	PSF+ Bulge+ Disk+ Bar	SB(rs)bc	B	20.14	-20.9	0.68	5.39e+10
NGC1302	PSF+ Bulge+ Disk+ Bar	(R)SB(r)0	B	21.43	-20.2	0.89	6.37e+10

(continued)

Table 2.1 (continued)

Galaxy name (1)	Best fit (2)	Hubble type (RC3) (3)	Bar type (RC3) (4)	D (Mpc) (5)	M_B (mag) (6)	$B - V$ (mag) (7)	M_* (M_\odot) (8)
NGC1309	PSF+Bulge+Disk	SA(s)bc	A	27.86	-20.5	0.44	1.46e+10
NGC1317	Bulge+Disk+Bar	SAB(r)a	AB	18.11	-20.2	0.89	6.42e+10
NGC1350	PSF+Bulge+Disk+Bar	(R')SB(r)ab	B	18.11	-21.1	0.87	1.38e+11
NGC1371	PSF+Bulge+Disk+Bar	SAB(rs)a	AB	18.32	-20.0	0.90	5.43e+10
NGC1385	PSF+Bar+Disk	SB(s)cd	B	18.75	-20.3	0.51	1.61e+10
NGC1511	Bulge+Disk	SAa:pec	A	16.18	-19.7	0.57	1.15e+10
NGC1559	PSF+Bar+Disk	SB(s)cd	B	15.32	-20.4	0.35	9.33e+09
NGC1703	PSF+Bulge+Disk	SB(r)b	B	18.64	-19.4	0.56	8.43e+09
NGC1792	PSF+Bulge+Disk	SA(rs)bc	A	14.57	-20.5	0.68	3.71e+10
NGC1808	PSF+Bulge+Disk+Bar	(R)SAB(s)a	AB	11.57	-19.9	0.81	3.57e+10
NGC1964	PSF+Bulge+Disk+Bar	SAB(s)b	AB	21.43	-20.8	0.77	6.54e+10
NGC2090	Bulge+Disk+Bar	SA(rs)c	A	10.93	-19.3	0.79	1.90e+10
NGC2139	Bulge+Disk	SAB(rs)cd	AB	24.00	-20.3	0.36	8.35e+09
NGC2196	PSF+Bulge+Disk	(R')SA(s)a	A	30.86	-21.0	0.81	9.22e+10
NGC2442	PSF+Bulge+Disk+Bar	SAB(s)bc:pec	AB	18.32	-20.8	0.82	8.28e+10
NGC2559	Bulge+Disk+Bar	SB(s)bc:pec	B	21.43	-21.0	—	—
NGC2566	Bulge+Disk	(R')SB(rs)ab:pec	B	22.61	-20.7	0.81	6.98e+10
NGC2775	PSF+Bulge+Disk	SA(r)ab	A	18.21	-20.6	0.90	9.46e+10
NGC3059	Bar+Disk	SB(rs)c	B	15.86	-20.1	0.68	2.52e+10
NGC3166	Bulge+Disk+Bar	SAB(rs)0	AB	23.57	-20.2	0.93	7.41e+10
NGC3169	PSF+Bulge+Disk	SA(s)a:pec	A	21.11	-20.3	0.85	6.09e+10
NGC3223	PSF+Bulge+Disk	SA(s)b	A	40.82	-21.9	0.82	2.36e+11
NGC3227	PSF+Bulge+Disk+Bar	SAB(s)a:pec	AB	22.07	-20.1	0.82	4.42e+10
NGC3261	PSF+Bulge+Disk+Bar	SB(rs)b	B	35.79	-21.3	—	—

NGC3275	PSF+Bulge+Disk+Bar	SB(r)ab	B	45.43	-21.2	-	-
NGC3319	PSF+Bar+Disk	SB(rs)cd	B	12.32	-19.4	0.41	4.76e+09
NGC3338	PSF+Bulge+Disk+Bar	SA(s)c	A	24.43	-20.6	0.59	2.67e+10
NGC3423	Bulge+Disk	SA(s)cd	A	11.68	-19.5	0.45	5.89e+09
NGC3504	Bulge+Disk+Bar	(R)SAB(s)ab	AB	21.43	-20.5	0.72	4.06e+10
NGC3513	Bulge+Disk+Bar	SB(rs)c	B	18.21	-19.9	0.43	7.52e+09
NGC3583	Bulge+Disk+Bar	SB(s)b	B	36.43	-20.8	-	-
NGC3596	PSF+Bulge+Disk	SAB(rs)c	AB	24.64	-19.6	-	-
NGC3646	PSF+Bulge+Disk	Ring	-	59.79	-22.9	0.65	2.82e+11
NGC3675	PSF+Bulge+Disk	SA(s)b	A	13.71	-20.2	-	-
NGC3684	PSF+Bulge+Disk	SA(rs)bc	A	25.07	-19.4	0.62	1.00e+10
NGC3686	PSF+Bulge+Disk+Bar	SB(s)bc	B	25.18	-19.6	0.57	9.97e+09
NGC3705	PSF+Bulge+Disk+Bar	SAB(r)ab	AB	18.21	-19.9	0.79	3.15e+10
NGC3726	PSF+Bulge+Disk+Bar	SAB(r)c	AB	18.21	-20.6	0.49	1.93e+10
NGC3810	PSF+Bulge+Disk	SA(rs)c	A	18.11	-20.1	0.58	1.72e+10
NGC3885	PSF+Bulge+Disk	SA(s)0	A	29.79	-19.6	0.95	4.62e+10
NGC3887	PSF+Bulge+Disk+Bar	SB(r)bc	B	20.68	-20.4	-	-
NGC3893	PSF+Bulge+Disk	SAB(rs)c	AB	18.21	-19.9	-	-
NGC3938	PSF+Bulge+Disk	SA(s)c	A	18.21	-20.0	0.52	1.23e+10
NGC3949	PSF+Bulge+Disk	SA(s)bc	AB	18.21	-19.9	0.45	8.66e+09
NGC4027	Bar+Disk	SB(s)dm	B	27.43	-20.6	0.54	2.25e+10
NGC4030	PSF+Bulge+Disk	SA(s)bc	A	27.75	-20.8	-	-
NGC4051	PSF+Bulge+Disk+Bar	SAB(rs)bc	AB	18.21	-20.0	0.65	1.95e+10
NGC4062	PSF+Bulge+Disk	SA(s)c	A	10.39	-19.5	0.76	2.07e+10
NGC4123	PSF+Bulge+Disk+Bar	SB(r)c	B	17.68	-19.8	0.61	1.50e+10
NGC4145	PSF+Bulge+Disk	SAB(rs)d	AB	22.18	-20.1	0.51	1.34e+10

(continued)

Table 2.1 (continued)

Galaxy name (1)	Best fit (2)	Hubble type (RC3) (3)	Bar type (RC3) (4)	D (Mpc) (5)	M_B (mag) (6)	$B - V$ (mag) (7)	M_* (M_\odot) (8)
NGC4151	PSF+Bulge+Disk+Bar	(R')SAB(rs)ab	AB	21.75	-20.1	0.73	$2.93e+10$
NGC4212	PSF+Bulge+Disk	SA(s)c	A	18.00	-20.4	0.67	$3.28e+10$
NGC4254	PSF+Bulge+Disk	SA(s)c	A	18.00	-22.6	0.57	$1.61e+11$
NGC4293	PSF+Bulge+Disk+Bar	(R)SB(s)0	B	18.21	-20.1	0.90	$5.94e+10$
NGC4303	Bulge+Disk+Bar	SAB(rs)bc	AB	16.29	-21.8	0.53	$6.76e+10$
NGC4314	PSF+Bulge+Disk+Bar	SB(rs)a	B	10.39	-19.8	0.85	$3.69e+10$
NGC4394	PSF+Bulge+Disk+Bar	(R)SB(r)b	B	18.00	-19.4	0.85	$2.61e+10$
NGC4414	PSF+Bulge+Disk+Bar	SA(rs)c	A	10.39	-20.0	0.84	$4.38e+10$
NGC4450	PSF+Bulge+Disk+Bar	SA(s)ab	A	18.00	-21.9	0.82	$2.22e+11$
NGC4487	PSF+Bulge+Disk+Bar	SAB(rs)cd	AB	21.32	-19.6	-	-
NGC4490	PSF+Bulge+Disk	SB(s)d,pec	B	8.36	-21.7	0.43	$4.10e+10$
NGC4527	Bulge+Disk+Bar	SAB(s)bc	AB	14.46	-21.5	0.86	$1.87e+11$
NGC4548	PSF+Bulge+Disk+Bar	SB(rs)b	B	18.00	-20.8	0.81	$7.85e+10$
NGC4593	PSF+Bulge+Disk+Bar	(R)SB(rs)b	B	42.32	-20.8	-	-
NGC4618	PSF+Bar+Disk	SB(rs)m	B	7.82	-19.3	0.44	$4.62e+09$
NGC4643	Bulge+Disk+Bar	SB(rs)0	B	27.54	-19.9	0.96	$6.49e+10$
NGC4647	Bulge+Disk	SAB(rs)c	AB	18.00	-19.8	0.65	$1.67e+10$
NGC4651	PSF+Bulge+Disk	SA(rs)c	A	18.00	-19.6	0.57	$1.05e+10$
NGC4654	Bulge+Disk	SAB(rs)cd	AB	18.00	-20.6	0.60	$2.99e+10$
NGC4665	PSF+Bulge+Disk+Bar	SB(s)0	B	19.18	-19.3	-	-
NGC4689	PSF+Bulge+Disk	SA(rs)bc	A	18.00	-20.7	0.65	$3.84e+10$
NGC4691	PSF+Bulge+Disk+Bar	(R)SB(s)0;pec	B	24.11	-19.6	0.58	$1.04e+10$
NGC4698	PSF+Bulge+Disk	SA(s)ab	A	18.00	-19.9	0.91	$5.15e+10$
NGC4699	Bulge+Disk+Bar	SAB(rs)b	AB	27.54	-21.5	0.89	$2.06e+11$
NGC4772	PSF+Bulge+Disk+Bar	SA(s)a	A	17.46	-19.4	0.92	$3.30e+10$

NGC4775	PSF+ <i>Bulge</i> + <i>Disk</i>	SA(s)d	A	28.50	-20.4	-	-
NGC4781	PSF+ <i>Bulge</i> + <i>Disk</i>	SB(rs)d	B	24.11	-20.8	-	-
NGC4818	PSF+ <i>Bulge</i> + <i>Disk</i> + <i>Bar</i>	SAB(rs)ab;pec	AB	23.04	-19.7	0.89	3.88e+10
NGC4856	PSF+ <i>Bulge</i> + <i>Disk</i> + <i>Bar</i>	SB(s)0	B	22.61	-20.2	0.99	9.04e+10
NGC4902	PSF+ <i>Bulge</i> + <i>Disk</i> + <i>Bar</i>	SB(r)b	B	42.00	-21.4	0.69	8.33e+10
NGC4930	PSF+ <i>Bulge</i> + <i>Disk</i> + <i>Bar</i>	SB(rs)b	B	37.50	-21.2	0.90	1.61e+11
NGC4939	PSF+ <i>Bulge</i> + <i>Disk</i>	SA(s)bc	A	47.46	-22.2	0.64	1.43e+11
NGC4941	PSF+ <i>Bulge</i> + <i>Disk</i>	(R)SAB(r)ab	AB	6.86	-19.4	0.84	2.50e+10
NGC4995	PSF+ <i>Bulge</i> + <i>Disk</i> + <i>Bar</i>	SAB(rs)b	AB	30.00	-20.6	0.87	8.25e+10
NGC5054	<i>Bulge</i> + <i>Disk</i>	SA(s)bc	A	29.25	-21.1	0.76	8.31e+10
NGC5085	<i>Bulge</i> + <i>Disk</i>	SA(s)c	A	30.96	-19.3	0.87	2.54e+10
NGC5101	PSF+ <i>Bulge</i> + <i>Disk</i> + <i>Bar</i>	(R)SB(rs)0	B	29.36	-20.8	1.00	1.69e+11
NGC5121	PSF+ <i>Bulge</i> + <i>Disk</i>	(R')SA(s)a	A	23.68	-19.4	0.95	3.68e+10
NGC5161	PSF+ <i>Bulge</i> + <i>Disk</i>	SA(s)c	A	35.89	-21.7	0.79	1.65e+11
NGC5247	PSF+ <i>Bulge</i> + <i>Disk</i>	SA(s)bc	A	23.79	-21.2	0.54	3.86e+10
NGC5371	PSF+ <i>Bulge</i> + <i>Disk</i> + <i>Bar</i>	SAB(rs)bc	AB	40.50	-22.1	0.70	1.74e+11
NGC5427	PSF+ <i>Bulge</i> + <i>Disk</i>	SA(s)c;pec	A	40.82	-21.2	0.57	4.61e+10
NGC5483	<i>Bulge</i> + <i>Disk</i> + <i>Bar</i>	SA(s)c	A	26.46	-20.3	-	-
NGC5643	PSF+ <i>Bulge</i> + <i>Disk</i> + <i>Bar</i>	SAB(rs)c	AB	18.11	-20.9	0.74	6.68e+10
NGC5676	PSF+ <i>Bulge</i> + <i>Disk</i>	SA(rs)bc	A	36.96	-21.5	0.68	9.01e+10
NGC5701	PSF+ <i>Bulge</i> + <i>Disk</i> + <i>Bar</i>	(R)SB(rs)0	B	27.96	-19.9	0.88	4.67e+10
NGC5713	PSF+ <i>Bulge</i> + <i>Disk</i>	SAB(rs)bc;pec	AB	32.57	-21.1	0.64	5.21e+10
NGC5850	PSF+ <i>Bulge</i> + <i>Disk</i> + <i>Bar</i>	SB(r)b	B	30.54	-21.5	0.79	1.37e+11
NGC5921	PSF+ <i>Bulge</i> + <i>Disk</i> + <i>Bar</i>	SB(r)bc	B	27.00	-20.6	0.66	3.51e+10
NGC5962	<i>Bulge</i> + <i>Disk</i> + <i>Bar</i>	SA(r)c	A	34.07	-20.9	0.64	4.43e+10
NGC6215	PSF+ <i>Bulge</i> + <i>Disk</i>	SA(s)c	A	21.96	-20.4	0.54	1.84e+10

(continued)

Table 2.1 (continued)

Galaxy name (1)	Best fit (2)	Hubble type (RC3) (3)	Bar type (RC3) (4)	D (Mpc) (5)	M_B (mag) (6)	$B - V$ (mag) (7)	M_* (M_\odot) (8)
NGC6221	Bulge+Disk+Bar	SB(s)bc:pec	B	20.79	-21.6	0.74	1.31e+11
NGC6300	PSF+Bulge+Disk+Bar	SB(rs)b	B	15.32	-20.3	0.78	4.49e+10
NGC6384	Bulge+Disk	SAB(r)bc	AB	28.50	-21.5	0.72	1.05e+11
NGC6753	PSF+Bulge+Disk+Bar	(R)SA(r)b	A	43.82	-21.6	0.83	1.81e+11
NGC6782	PSF+Bulge+Disk+Bar	(R)SAB(r)a	AB	54.43	-21.4	-	-
NGC6902	PSF+Bulge+Disk	SA(r)b	A	38.25	-21.2	0.71	8.12e+10
NGC6907	PSF+Bulge+Disk+Bar	SB(s)bc	B	46.07	-21.8	0.69	1.21e+11
NGC7083	PSF+Bulge+Disk	SA(s)bc	A	41.46	-21.8	0.65	1.05e+11
NGC7205	PSF+Bulge+Disk	SA(s)bc	A	21.96	-20.7	0.60	3.11e+10
NGC7213	PSF+Bulge+Disk	SA(s)a	A	23.57	-21.0	0.89	1.26e+11
NGC7217	PSF+Bulge+Disk	(R)SA(r)ab	A	17.14	-20.5	0.90	8.38e+10
NGC7412	PSF+Bulge+Disk+Bar	SB(s)b	B	22.61	-20.2	0.53	1.50e+10
NGC7479	PSF+Bulge+Disk+Bar	SB(s)c	B	34.71	-21.7	0.75	1.44e+11
NGC7552	Bulge+Disk+Bar	(R')SB(s)ab	B	20.89	-20.5	0.68	3.49e+10
NGC7723	PSF+Bulge+Disk+Bar	SB(r)b	B	25.39	-20.5	0.73	4.32e+10
NGC7727	PSF+Bulge+Disk	SAB(s)a:pec	AB	24.96	-20.8	0.91	1.13e+11
NGC7741	Bulge+Disk+Bar	SB(s)cd	B	13.18	-19.3	0.53	6.67e+09

Columns are: (1) Galaxy name, (2) The best fit chosen based on the criteria outlined in Sect. 2.3.3, (3) Hubble type from RC3 (de Vaucouleurs et al. 1991), (4) RC3 bar type, which is based on visual inspection of optical images and runs as 'B' = 'strongly barred', 'AB' = 'weakly barred', and 'A' = 'unbarred'. (5) The distance in Mpc from the Nearby Galaxies Catalog (Tully 1988) scaled to a Hubble constant of $70 \text{ km s}^{-1} \text{ Mpc}^{-1}$. Distances are adjusted assuming the Galaxy is retarded by 300 km s^{-1} from the universal expansion by the mass of the Virgo Cluster. Exceptions are NGC 6753, NGC 6782, and NGC 6907 where distances are from RC3, NGC 3504 where the distance is from Kenney et al. (1993), and NGC 4314 where the distance is from Benedict et al. (1996). (6) Absolute B -band magnitude from Hyperleda. Corrections have been applied for galactic and internal extinction. Galactic absorption is computed based on Schlegel et al. (1998). Internal extinction is corrected for following Bottinelli et al. (1995). K-correction co-efficients are drawn from RC2 (de Vaucouleurs et al. 1976). (7) $B - V$ color from Hyperleda. Corrections for extinction and k-correction have been applied as in column 6. (8) Stellar mass, calculated as outlined in Sect. 2.2.2

dynamical (Drory et al. 2004) techniques. Typical errors are within a factor of two to three. Salucci et al. (2008) derive disk masses with both photometric and kinematic methods and find the two methods are equivalent on average. For a sample of 18, they find an rms scatter of 0.23 dex, while on an individual basis the deviation can be as high as 0.5 dex.

We used this relation to compute stellar masses for 126 of 143 (88 %) objects. The remainder did not have $B - V$ colors available in the Hyperleda database or RC3. The mass distribution is summarized in Fig. 2.3. Individual masses are listed in Table 2.1. This sample of 126 galaxies is referenced henceforth as sample S2.

2.3 Method and Analysis

The structural properties of galaxy components, such as bulges, disks, and bars can be derived through the decomposition of the 2D light distribution, taking into account the PSF. There are several algorithms for 2D luminosity decomposition, including GIM2D (Simard et al. 2002), GALFIT (Peng et al. 2002), and BUDDA (de Souza et al. 2004). The latter two allow bulge-disk-bar decomposition, while the former only allows bulge-disk decomposition.

Most previous work has addressed 2D bulge-disk decomposition only. Allen et al. (2006), for example, performed bulge-disk decomposition of B -band images with GIM2D on 10,095 galaxies from the Millennium Galaxy Catalog (Liske et al. 2003; Driver et al. 2005). However, recent work (e.g., Laurikainen et al. 2005) has shown that the B/T ratio can be artificially inflated in a barred galaxy unless the bar component is included in the 2D decomposition. The fact that most ($\geq 60\%$) bright spiral galaxies are barred in the NIR (Eskridge et al. 2000; Laurikainen et al. 2004; MJ07; Menéndez-Delmestre et al. 2007), further warrants the inclusion of the bar. Another advantage of bulge-disk-bar decomposition is that it allows us to constrain the properties of the bar itself, and to constrain scenarios of bar-driven evolution (see Sect. 2.1).

Motivated by these considerations, several studies have tackled the problem of 2D bulge-disk-bar decomposition. Laurikainen et al. (2005, 2007) have developed a 2D multicomponent decomposition code designed to model bulges, disks, primary and secondary bars, and lenses; they apply Sérsic functions to bulges and use either Sérsic or Ferrers functions to describe bars and lenses. Reese et al. (2007) have written a non-parametric algorithm to model bars in ~ 70 I -band images. Gadotti and Kauffmann (2007) are performing 2D bulge-disk-bar and bulge-disk decomposition of 1,000 barred and unbarred galaxies from SDSS with the BUDDA software.

In this study, we perform 2D two-component bulge-disk decomposition and three-component bulge-disk-bar decomposition of the OSUBSGS sample with GALFIT. We note that Laurikainen et al. (2007) have also performed bulge-disk-bar decomposition on the OSUBSGS sample. However, there are also important complementary differences between our study and theirs. The decomposition

algorithm and tests on the robustness performed in our study are different (see Sects. 2.3 and 2.4). Furthermore, unlike Laurikainen et al. (2007), we also compare the bulge-to-total ratio (B/T) with predictions from hierarchical models of galaxy evolution (Sect. 2.5), and also present the distribution of bar-to-total ratio (Bar/T).

2.3.1 Image Preparation

Running GALFIT on an image requires initial preparation. The desired fitting region and sky background must be known, and the PSF image, bad pixel mask (if needed), and pixel noise map must be generated. We addressed these issues as follows: (1) The GALFIT fitting region must be large enough to include the outer galaxy disk, as well as some sky region. Since cutting out empty regions of sky can drastically reduce GALFIT run-time, a balance was sought between including the entire galaxy and some decent sky region, while excluding large extraneous blank sky areas. (2) It is possible for GALFIT to fit the sky background, but this is not recommended. When the sky is a free parameter, the wings of the bulge Sérsic profile can become inappropriately extended, resulting in a Sérsic index that is too high. Sky backgrounds were measured separately and designated as fixed parameters; (3) GALFIT requires a PSF image to correct for seeing effects. Statistics of many stars in each frame can be used to determine an average PSF. However, many of our images contain merely a few stars. Instead, a high S/N star from each frame was used as a PSF. (4) We used ordered lists of pixel coordinates to make bad pixel masks, which are useful for blocking out bright stars and other image artifacts. (5) We had GALFIT internally calculate pixel noise maps for an image from the noise associated with each pixel. Noise values are determined from image header information concerning gain, read noise, exposure time, and the number of combined exposures.

2.3.2 Decomposition Steps

Figure 2.4 summarizes our method of decomposition, which we now detail. GALFIT requires initial guesses for each component it fits. It uses a Levenberg–Marquardt downhill-gradient algorithm to determine the minimum χ^2 based on the input guesses. GALFIT continues iterating until the χ^2 changes by less than $5e-04$ for five iterations (Peng et al. 2002). We recognize that a drawback to any least-squares method is that a local minimum, rather than a global minimum, in χ^2 space may be converged upon.

We explore this possibility with multiple tests described in Sect. 2.4. We adopted an iterative process, involving three separate invocations of GALFIT, to perform 1-component, 2-component, and 3-component decomposition:

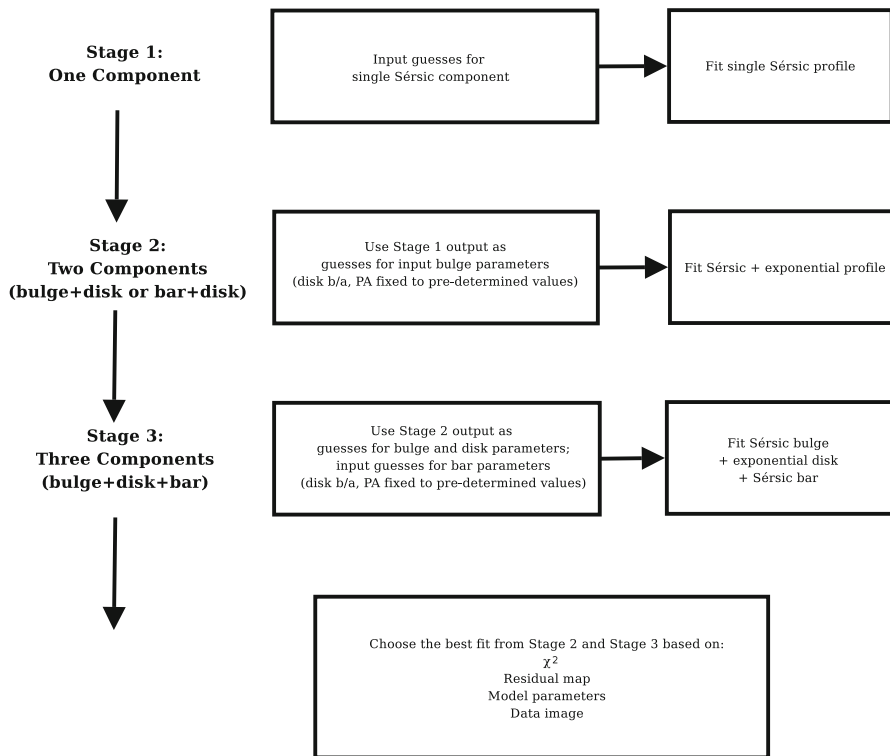


Fig. 2.4 An overview of the method of decomposition. All images are subjected to Stages 1, 2, and 3. Either the best fit of Stage 2 or Stage 3 is chosen as the best model

1. Stage 1 (single Sérsic): In Stage 1, a single Sérsic¹ component is fitted to the galaxy. This serves the purpose of measuring the total luminosity, which is conserved in later Stages, and the centroid of the galaxy, which is invariant in later fits.
2. Stage 2 (exponential plus Sérsic): In Stage 2, the image is fit with the sum of an exponential disk and a Sérsic component. During the Stage 2 fit, the disk b/a and PA are held constant at values, which we take from the published ellipse fits of MJ07, as well as ellipse fits of our own. This procedure reduces the number of free parameters in the fit by fixing the disk b/a and PA , which are easily measurable parameters. It also prevents GALFIT from confusing the disk and bar, and artificially stretching the disk along the bar PA in an attempt to mimic

¹The functional form for the Sérsic profile is $\Sigma(r) = \Sigma_e \exp \left[-b_n \left(\left(\frac{r}{r_e} \right)^{1/n} - 1 \right) \right]$. Σ_e is the pixel surface brightness at effective radius r_e , and n is the Sérsic index. b_n is a coupled to n and is not a free parameter.

the bar. As initial guesses for the Sérsic component in Stage 2, the output of Stage 1 is used. The Sérsic component in Stage 2 usually represents the bulge, in which case Stage 2 corresponds to a standard bulge-disk decomposition.

However, in a few rare cases, where the galaxy has just a bar and a disk, the Sérsic component in Stage 2 represents a bar. The latter is recognizable by a low Sérsic index and large half-light radius.

3. Stage 3 (exponential plus two Sérsic components): In Stage 3, a three-component model consisting of an exponential disk, a Sérsic bulge, and a Sérsic bar is fit. As suggested by Peng et al. (2002), the bar can be well described by an elongated, low-index Sérsic ($n < 1$) profile. As in Stage 2, the disk b/a and PA are held constant at values predetermined from ellipse fits. We provide initial guesses for the bar b/a and PA , based on ellipse fits of the images from MJ07 or analysis of the images in DS9. We provide GALFIT with input guesses for the bulge parameters, based on the output from Stage 2. In principle, it is also possible to generate reasonable guess parameters for the bulge and disk from a bulge-disk decomposition on a $1D$ profile taken along a select PA . As described in Sect. 2.4.3, we also experiment with initial guesses derived in this way, and find that the final convergence solution is the same. We also note that GALFIT fixes the bulge b/a and does not allow it to vary with radius, while real bulges may have a varying b/a . We tested the impact of fixed and varying bulge b/a on the derived B/T (Sect. 2.4.1) and find that there is no significant change in B/T .

For objects with central point sources, the bulge Sérsic index in the Stage 2 and Stage 3 models can be inadvertently overestimated unless an extra nuclear component is added to the model. Balcells et al. (2003) note that for galaxies imaged both from the ground and *HST*, the combination of unresolved central sources and seeing effects mimic high-index bulge Sérsic profiles in the ground images. Depending on sample and resolution, the frequency of central sources can range from 50 to 90 % (Ravindranath et al. 2001; Böker et al. 2002; Balcells et al. 2003). Ravindranath et al. (2001) find a frequency of 50 % in early type (E, S0, S0/a) galaxies, while Böker et al. (2002) measure a frequency of 75 % for spirals with Hubble types Scd to Sm. Balcells et al. (2003) determine a frequency of 84 % for S0-Sbc galaxies imaged with *HST*. Our dataset most closely resembles the latter sample, so we might expect that, as an upper limit, a similar fraction of our galaxies will need to be corrected with an extra compact component.

We added point sources as third or fourth components to the initial models. For those cases where the model successfully converged with the extra component, the images were visually inspected to verify the presence of a central bright source. Sometimes, the model converged to significantly different and unreasonable parameters for all components. Other times, the model would converge to a very dim point source without changing any of the other model parameters. Where new model parameters were not unreasonable and not identical to the case without the point source, the new model was adopted. This was the case for 111 of 143 (78 %) of our sample. The point sources contribute less than 1, 3, and 5 % of the total luminosity 55, 86, and 95 % of the time, respectively. As the point sources take up

such a small fraction of the light distribution, their contribution is folded back into B/T in all cases where a point source was modeled. Inclusion of the point source reduced bulge index by ~ 0.8 for both barred and unbarred galaxies. Such a change is expected based on the above discussion. The decline in bulge index caused a minor decrease in B/T ; on the mean, this change was 1.04 % for barred galaxies and 0.32 % for unbarred galaxies. For barred galaxies, this light most primarily added to D/T rather than Bar/T .

It is important to recognize the physical significance of the added nuclear components. We began by determining which objects show evidence for AGN activity. The sample was checked against the catalog of Ho et al. (1997), the Véron Catalog of Quasars & AGN, 12th Edition (Véron-Cetty and Véron 2006), and NED. Of the 111 objects fit with point sources, 43 (39 %) contain AGN. An additional 20 (18 %) possess HII nuclei according to Ho et al. (1997) and visibly show bright compact nuclei. The remaining 48 (43 %) probably contain neither AGN nor HII nuclei, but could house nuclear star clusters. For these objects, we visually inspected the images to ensure there was a bright compact source at the center. We are confident that the fitted point source components have physical counterparts in the data images.

GALFIT also allows a diskiness/boxiness parameter to be added to any Sérsic or exponential profile. We did not use this parameter for any bulge or disk profiles. Bars in general have boxy isophotes, and we could have included the diskiness/boxiness parameter in the bar profiles. However, it was found that adding boxiness to the bar did not change any model parameters, including fractional luminosities B/T , D/T , and Bar/T , by more than a small percentage, even though the appearance of the residual images improved in some cases due to the change in bar shape. Consequently, we chose to neglect bar boxiness altogether.

2.3.3 *Choosing the Best Fit Between Stage 2 and Stage 3*

All objects in our sample were subjected to Stages 1, 2, and 3. Depending on whether a galaxy with a bulge is unbarred or barred, its best fit should be taken from the Stage 2 bulge-disk decomposition or the Stage 3 bulge-disk-bar decomposition, respectively. For objects with prominent bars, it is obvious that the Stage 3 model provides the best fit. However, it is more difficult to decide between Stage 2 versus Stage 3 fits in galaxies which host weak bars with no strong visual signature. In practice, we therefore applied the set of criteria below to each galaxy in order to select between the Stage 2 bulge-disk decomposition and Stage 3 bulge-disk-bar decomposition. Table 2.1 lists the model chosen for each galaxy. Table 2.2 summarizes the model parameters from the best fits.

For completeness, we note that for the few rare galaxies (see Sect. 2.3.2) that have just a bar and a disk, the choice of a final solution is between the Stage 2 bar-disk decomposition and Stage 3 bulge-disk-bar decomposition. The same guidelines below can be used to identify the best model.

Table 2.2 Parameters from 2D luminosity decomposition for sample S1 (N=143)

Galaxy name (1)	Best fit (2)	B/T % (3)	D/T % (4)	Bar/T % (5)	B/D (6)	Bulge r_c '' (7)	Bulge r_e kpc (8)	Bulge n (9)	Disk h '' (10)	Disk h kpc (11)	$Bar r_e$ '' (12)	$Bar r_e$ kpc (13)	$Bar n$ (14)
ESO138-10	PSF+Bulge+Disk	16.25	83.75	—	0.19	10.94	0.83	2.07	27.10	2.06	—	—	—
IC0239	PSF+Bulge+Disk+Bar	2.45	92.65	4.91	0.03	6.63	0.49	0.23	34.56	2.54	13.95	1.02	0.19
IC4444	Bulge+Disk	31.97	68.03	—	0.47	7.94	1.10	2.33	17.67	2.45	—	—	—
IC5325	PSF+Bulge+Disk	6.79	93.21	—	0.07	15.17	1.42	1.75	23.18	2.17	—	—	—
NGC0150	PSF+Bulge+Disk+Bar	5.72	81.18	13.11	0.07	4.22	0.42	0.05	33.57	3.33	17.82	1.77	0.39
NGC0157	PSF+Bulge+Disk	2.29	97.71	—	0.02	3.44	0.37	0.44	31.82	3.43	—	—	—
NGC0210	Bulge+Disk+Bar	30.07	48.54	21.39	0.62	4.81	0.50	1.71	83.21	8.71	29.41	3.08	0.31
NGC0278	PSF+Bulge+Disk	4.23	95.77	—	0.04	3.46	0.21	0.57	13.48	0.82	—	—	—
NGC0289	PSF+Bulge+Disk+Bar	8.83	85.99	5.18	0.10	4.91	0.49	0.46	20.28	2.03	18.90	1.89	0.04
NGC0428	PSF+Bulge+Disk+Bar	5.50	71.64	22.86	0.08	9.27	0.71	0.38	32.55	2.51	30.70	2.36	0.37
NGC0488	PSF+Bulge+Disk	21.72	78.28	—	0.28	9.91	1.49	3.07	38.94	5.87	—	—	—
NGC0578	PSF+Bulge+Disk+Bar	2.05	93.63	4.32	0.02	4.19	0.42	0.56	40.73	4.10	14.95	1.50	0.18
NGC0613	PSF+Bulge+Disk+Bar	13.14	56.97	29.90	0.23	6.12	0.55	1.05	44.69	4.04	62.49	5.65	0.53
NGC0685	Bar+Disk	—	96.53	3.47	—	—	—	—	41.24	3.24	20.68	1.62	0.16
NGC0779	Bulge+Disk+Bar	16.18	57.69	26.13	0.28	6.04	0.54	2.31	38.74	3.46	29.00	2.59	0.25
NGC0864	PSF+Bulge+Disk+Bar	2.77	86.88	10.35	0.03	3.52	0.36	0.66	39.54	4.08	21.07	2.17	0.37
NGC0908	PSF+Bulge+Disk	8.86	91.14	—	0.10	7.18	0.66	1.62	48.96	4.50	—	—	—
NGC1042	PSF+Bulge+Disk	3.00	97.00	—	0.03	5.91	0.51	0.09	39.83	3.43	—	—	—
NGC1073	PSF+Bulge+Disk+Bar	2.36	79.58	18.06	0.03	5.47	0.43	0.41	50.02	3.93	34.24	2.69	0.83
NGC1084	PSF+Bulge+Disk	5.23	94.77	—	0.06	3.24	0.29	0.77	18.68	1.65	—	—	—
NGC1087	Bar+Disk	—	93.13	6.87	—	—	—	—	28.55	2.80	7.79	0.76	1.27
NGC1187	PSF+Bulge+Disk+Bar	6.94	64.96	28.10	0.11	4.81	0.41	1.57	38.20	3.22	51.85	4.37	0.72

NGC1241	PSF+ Bulge+ Disk+ Bar	11.70	69.10	19.21	0.17	2.61	0.36	0.91	27.69	3.79	17.89	2.45	0.49
NGC1300	PSF+ Bulge+ Disk+ Bar	11.04	74.94	14.02	0.15	4.63	0.45	1.19	63.53	6.16	65.89	6.39	0.25
NGC1302	PSF+ Bulge+ Disk+ Bar	17.65	63.79	18.57	0.28	4.96	0.51	2.01	44.92	4.63	20.44	2.11	0.76
NGC1309	PSF+ Bulge+ Disk	27.07	72.93	—	0.37	10.86	1.45	2.27	16.67	2.23	—	—	—
NGC1317	Bulge+ Disk+ Bar	13.86	41.48	44.65	0.33	3.99	0.35	1.94	47.37	4.13	20.22	1.76	2.19
NGC1350	PSF+ Bulge+ Disk+ Bar	19.52	69.99	10.50	0.28	7.41	0.65	1.59	52.77	4.61	51.07	4.46	0.31
NGC1371	PSF+ Bulge+ Disk+ Bar	12.46	80.16	7.38	0.16	5.17	0.46	1.11	29.34	2.59	18.92	1.67	0.36
NGC1385	PSF+ Bar+ Disk	—	75.54	24.46	—	—	—	—	28.69	2.59	15.63	1.41	1.28
NGC1511	Bulge+ Disk	28.47	71.53	—	0.40	27.78	2.17	1.35	23.99	1.87	—	—	—
NGC1559	PSF+ Bar+ Disk	—	97.06	2.94	—	—	—	—	31.16	2.30	9.84	0.73	0.53
NGC1703	PSF+ Bulge+ Disk	6.32	93.68	—	0.07	2.83	0.25	0.56	18.24	1.64	—	—	—
NGC1792	PSF+ Bulge+ Disk	2.65	97.35	—	0.03	3.72	0.26	0.84	38.50	2.71	—	—	—
NGC1808	PSF+ Bulge+ Disk+ Bar	3.92	74.27	21.82	0.05	2.78	0.16	0.45	38.78	2.17	5.71	0.32	0.67
NGC1964	PSF+ Bulge+ Disk+ Bar	41.78	49.87	8.35	0.84	8.31	0.86	2.58	18.59	1.92	8.05	0.83	0.05
NGC2090	Bulge+ Disk+ Bar	14.67	58.39	26.94	0.25	17.68	0.93	2.19	160.02	8.45	33.74	1.78	0.43
NGC2139	Bulge+ Disk	15.16	84.84	—	0.18	8.27	0.95	1.53	18.12	2.09	—	—	—
NGC2196	PSF+ Bulge+ Disk	46.38	53.62	—	0.86	13.42	1.99	2.38	28.38	4.21	—	—	—
NGC2442	PSF+ Bulge+ Disk+ Bar	13.33	62.47	24.19	0.21	4.78	0.42	1.68	78.46	6.93	60.15	5.31	0.24
NGC2559	Bulge+ Disk+ Bar	6.98	81.64	11.37	0.09	4.01	0.41	1.38	34.65	3.58	21.40	2.21	0.24
NGC2566	Bulge+ Disk	22.71	77.29	—	0.29	1.74	0.19	4.42	23.05	2.51	—	—	—
NGC2775	PSF+ Bulge+ Disk	60.87	39.13	—	1.56	47.35	4.16	4.85	28.09	2.47	—	—	—
NGC3059	Bar+ Disk	—	90.68	9.32	—	—	—	—	64.22	4.91	23.94	1.83	1.43
NGC3166	Bulge+ Disk+ Bar	24.97	50.74	24.29	0.49	3.25	0.37	0.81	20.14	2.29	13.85	1.57	0.53

(continued)

Table 2.2 (continued)

Galaxy name	Best fit	B/T	D/T	Bar/T	B/D	Bulge r_e	Bulge r_e	Bulge n	Disk h	Disk h	$Bar r_e$	$Bar r_e$	$Bar n$
(1)	(2)	(3)	(4)	(5)	(6)	"	kpc	(9)	"	(11)	"	kpc	(14)
NGC3169	PSF+Bar+Disk	38.53	61.47	—	0.63	11.01	1.12	2.41	55.12	5.60	—	—	—
NGC3223	PSF+Bar+Disk	11.71	88.29	—	0.13	5.39	1.05	1.74	29.05	5.68	—	—	—
NGC3227	PSF+Bar+Disk+Bar	10.78	45.23	44.00	0.24	4.84	0.51	0.32	44.67	4.75	39.51	4.20	1.27
NGC3261	PSF+Bar+Disk+Bar	15.06	70.15	14.79	0.21	2.95	0.51	1.96	28.89	4.96	14.19	2.43	1.05
NGC3275	PSF+Bar+Disk+Bar	14.15	63.44	22.41	0.22	2.21	0.48	1.85	28.25	6.14	20.75	4.51	0.94
NGC3319	PSF+Bar+Disk	—	91.41	8.59	—	—	—	—	66.08	3.93	14.60	0.87	0.43
NGC3338	PSF+Bar+Disk+Bar	5.29	81.96	12.75	0.06	4.39	0.52	0.76	36.42	4.28	20.62	2.42	0.39
NGC3423	Bulge+Disk	28.10	71.90	—	0.39	24.09	1.36	2.39	31.21	1.76	—	—	—
NGC3504	Bulge+Disk+Bar	23.15	39.49	37.37	0.59	2.37	0.24	1.04	29.55	3.05	26.02	2.69	0.78
NGC3513	Bulge+Disk+Bar	4.45	92.08	3.47	0.05	10.73	0.94	1.46	33.18	2.91	18.32	1.61	0.08
NGC3583	Bulge+Disk+Bar	8.62	53.40	37.98	0.16	1.29	0.23	1.28	21.78	3.80	14.89	2.60	0.68
NGC3596	PSF+Bar+Disk	12.15	87.85	—	0.14	5.34	0.63	0.67	18.54	2.20	—	—	—
NGC3646	PSF+Bar+Disk	13.53	86.47	—	0.16	3.60	1.03	1.20	26.01	7.41	—	—	—
NGC3675	PSF+Bar+Disk	44.42	55.58	—	0.80	28.41	1.88	2.66	47.12	3.12	—	—	—
NGC3684	PSF+Bar+Disk	26.92	73.08	—	0.37	11.43	1.38	2.15	15.96	1.92	—	—	—
NGC3686	PSF+Bar+Disk+Bar	3.02	95.00	1.98	0.03	4.39	0.53	0.66	27.57	3.34	21.32	2.58	0.03
NGC3705	PSF+Bar+Disk+Bar	27.73	59.20	13.07	0.47	8.62	0.76	1.83	37.77	3.32	30.00	2.63	0.07
NGC3726	PSF+Bar+Disk+Bar	3.09	95.10	1.81	0.03	5.64	0.50	0.53	49.58	4.35	41.09	3.61	0.05
NGC3810	PSF+Bar+Disk	38.43	61.57	—	0.62	12.35	1.08	1.28	23.78	2.08	—	—	—
NGC3885	PSF+Bar+Disk	27.10	72.90	—	0.37	3.13	0.45	0.46	11.94	1.71	—	—	—
NGC3887	PSF+Bar+Disk+Bar	4.19	83.01	12.80	0.05	5.27	0.53	1.01	42.69	4.25	37.62	3.75	0.62
NGC3893	PSF+Bar+Disk	54.61	45.39	—	1.20	20.05	1.76	2.05	23.40	2.05	—	—	—
NGC3938	PSF+Bar+Disk	7.30	92.70	—	0.08	6.43	0.56	1.18	32.84	2.88	—	—	—
NGC3949	PSF+Bar+Disk	7.75	92.25	—	0.08	4.67	0.41	0.64	15.22	1.34	—	—	—

Table 2.2 (continued)

Galaxy name	Best fit	B/T %	D/T %	Bar/ T %	B/D	Bulge r_e "	Bulge r_e kpc	Bulge n	Disk h "	Disk h kpc	Bar r_e "	Bar r_e kpc	Bar n
(1)	(2)	(3)	(4)	(5)	(6)	(7)	(8)	(9)	(10)	(11)	(12)	(13)	(14)
NGC4654	Bulge+Disk	1.74	98.26	—	0.02	3.78	0.33	0.93	30.16	2.62	—	—	—
NGC4665	PSF+Bulge+Disk+Bar	14.74	67.38	17.89	0.22	6.92	0.64	1.12	50.48	4.66	30.68	2.83	0.70
NGC4689	PSF+Bulge+Disk	5.22	94.78	—	0.06	6.97	0.61	1.14	41.85	3.63	—	—	—
NGC4691	PSF+Bulge+Disk+Bar	15.80	69.09	15.11	0.23	11.62	1.35	0.61	33.90	3.93	24.99	2.90	0.42
NGC4698	PSF+Bulge+Disk	21.72	78.28	—	0.28	6.78	0.59	1.78	28.34	2.46	—	—	—
NGC4699	Bulge+Disk+Bar	19.93	76.48	3.59	0.26	2.62	0.35	2.08	15.93	2.11	13.49	1.79	0.02
NGC4772	PSF+Bulge+yDisk+Bar	34.25	51.55	14.20	0.66	9.29	0.78	1.49	58.16	4.90	52.58	4.43	0.50
NGC4775	PSF+Bulge+Disk	32.85	67.15	—	0.49	21.43	2.94	1.75	18.48	2.53	—	—	—
NGC4781	PSF+Bulge+yDisk	10.18	89.82	—	0.11	12.02	1.39	0.94	32.82	3.81	—	—	—
NGC4818	PSF+Bulge+Disk+Bar	7.04	73.74	19.22	0.10	2.82	0.31	0.47	36.31	4.03	16.38	1.82	0.51
NGC4856	PSF+Bulge+Disk+Bar	27.44	61.22	11.35	0.45	5.95	0.65	1.53	30.61	3.33	17.07	1.86	0.44
NGC4902	PSF+Bulge+Disk+Bar	5.59	84.44	9.97	0.07	4.31	0.87	0.85	29.24	5.88	14.13	2.84	0.39
NGC4930	PSF+Bulge+Disk+Bar	23.74	61.29	14.98	0.39	6.46	1.16	1.37	45.02	8.09	32.96	5.92	0.38
NGC4939	PSF+Bulge+Disk	21.37	78.63	—	0.27	9.52	2.16	2.78	32.14	7.29	—	—	—
NGC4941	PSF+Bulge+Disk	15.08	84.92	—	0.18	4.30	0.14	0.84	23.23	0.77	—	—	—
NGC4995	PSF+Bulge+Disk+Bar	6.62	87.18	6.20	0.08	4.14	0.60	0.05	19.56	2.82	18.03	2.60	0.34
NGC5054	Bulge+Disk	9.64	90.36	—	0.11	5.28	0.74	2.42	52.65	7.40	—	—	—
NGC5085	Bulge+Disk	6.04	93.96	—	0.06	5.53	0.82	1.48	33.88	5.04	—	—	—
NGC5101	PSF+Bulge+Disk+Bar	32.63	48.31	19.06	0.68	7.61	1.07	2.28	28.39	4.00	37.85	5.34	0.31
NGC5121	PSF+Bulge+Disk	36.43	63.57	—	0.57	4.68	0.53	2.41	15.62	1.78	—	—	—
NGC5161	PSF+Bulge+Disk	27.14	72.86	—	0.37	20.54	3.54	1.47	43.98	7.57	—	—	—
NGC5247	PSF+Bulge+Disk	7.54	92.46	—	0.08	8.46	0.97	1.04	50.85	5.82	—	—	—
NGC5371	PSF+Bulge+Disk+Bar	8.60	76.08	15.32	0.11	3.13	0.61	1.29	55.81	10.83	23.03	4.47	1.05
NGC5427	PSF+Bulge+Disk	7.76	92.24	—	0.08	4.74	0.93	0.60	24.59	4.81	—	—	—

NGC5483	Bulge+Disk+Bar	0.98	91.28	7.73	0.01	3.23	0.41	1.22	23.25	2.96	8.74	1.11	0.32
NGC5643	PSF+Bulge+Disk+Bar	8.21	81.78	10.01	0.10	5.68	0.50	2.14	45.30	3.95	48.58	4.24	0.43
NGC5676	PSF+Bulge+Disk	6.67	93.33	—	0.07	3.71	0.66	1.29	23.10	4.09	—	—	—
NGC5701	PSF+Bulge+Disk+Bar	24.43	63.47	12.09	0.38	11.13	1.50	2.41	70.67	9.50	26.01	3.50	0.40
NGC5713	PSF+Bulge+Disk	33.40	66.60	—	0.50	15.59	2.44	1.84	18.52	2.90	—	—	—
NGC5850	PSF+Bulge+Disk+Bar	14.76	63.74	21.50	0.23	6.22	0.91	1.58	72.24	10.59	46.05	6.75	0.90
NGC5921	PSF+Bulge+Disk+Bar	10.43	70.50	19.06	0.15	2.55	0.33	1.97	40.88	5.31	35.05	4.55	0.92
NGC5962	Bulge+Disk+Bar	10.30	78.82	10.88	0.13	2.33	0.38	1.37	14.56	2.38	13.85	2.26	0.02
NGC6215	PSF+Bulge+Disk	6.95	93.05	—	0.07	2.55	0.27	0.96	14.02	1.48	—	—	—
NGC6221	Bulge+Disk+Bar	5.27	81.98	12.76	0.06	3.16	0.32	2.73	51.47	5.15	19.33	1.93	0.87
NGC6300	PSF+Bulge+Disk+Bar	5.98	86.55	7.47	0.07	5.43	0.40	1.44	47.08	3.48	31.64	2.34	0.30
NGC6384	Bulge+Disk	27.92	72.08	—	0.39	15.66	2.14	3.13	40.05	5.49	—	—	—
NGC6753	PSF+Bulge+Disk+Bar	5.08	72.91	22.02	0.07	1.50	0.31	0.94	19.17	4.02	7.88	1.65	0.80
NGC6782	PSF+Bulge+Disk+Bar	26.27	51.75	21.98	0.51	3.90	1.01	1.10	27.14	7.05	19.27	5.00	0.38
NGC6902	PSF+Bulge+Disk	40.55	59.45	—	0.68	12.68	2.32	3.03	30.13	5.52	—	—	—
NGC6907	PSF+Bulge+Disk+Bar	10.32	63.12	26.56	0.16	3.49	0.77	1.10	28.99	6.39	23.37	5.15	0.33
NGC7083	PSF+Bulge+Disk	13.23	86.77	—	0.15	5.87	1.17	1.37	23.26	4.62	—	—	—
NGC7205	PSF+Bulge+Disk	6.08	93.92	—	0.06	4.70	0.50	0.88	31.03	3.28	—	—	—
NGC7213	PSF+Bulge+Disk	65.74	34.26	—	1.92	19.55	2.22	2.68	63.19	7.17	—	—	—
NGC7217	PSF+Bulge+Disk	53.71	46.29	—	1.16	21.07	1.74	2.21	26.84	2.22	—	—	—
NGC7412	PSF+Bulge+Disk+Bar	4.09	68.60	27.31	0.06	2.84	0.31	1.28	23.58	2.57	35.06	3.81	1.20
NGC7479	PSF+Bulge+Disk+Bar	8.76	63.51	27.72	0.14	6.00	1.00	1.09	37.59	6.26	40.63	6.77	0.47
NGC7552	Bulge+Disk+Bar	23.44	61.08	15.48	0.38	2.70	0.27	0.64	17.54	1.76	42.05	4.23	0.24
NGC7723	PSF+Bulge+Disk+Bar	5.11	85.03	9.85	0.06	2.61	0.32	0.54	21.70	2.65	21.81	2.66	0.90
NGC7727	PSF+Bulge+Disk	41.77	58.23	—	0.72	8.31	1.00	2.02	24.46	2.94	—	—	—
NGC7741	Bulge+Disk+Bar	3.09	89.02	7.90	0.03	9.51	0.60	0.31	60.98	3.88	30.02	1.91	0.40

Columns are: (1) Galaxy name. (2) The best fit chosen based on the criteria outlined in Sect. 2.3.3. (3) Bulge-to-total light ratio. If a PSF is included in the model, the contribution from the PSF is also added in. (4) Disk-to-total light ratio. (5) Bar-to-total light ratio. (6) Bulge-to-disk ratio (7) Bulge effective radius in arcseconds. (8) Bulge effective radius in kpc. (9) Bulge Sérsic index. (10) Disk Sérsic index. (11) Disk scalelength in arcseconds. (12) Bar effective radius in arcseconds. (13) Bar Bulge effective radius in kpc. (14) Bar Sérsic index

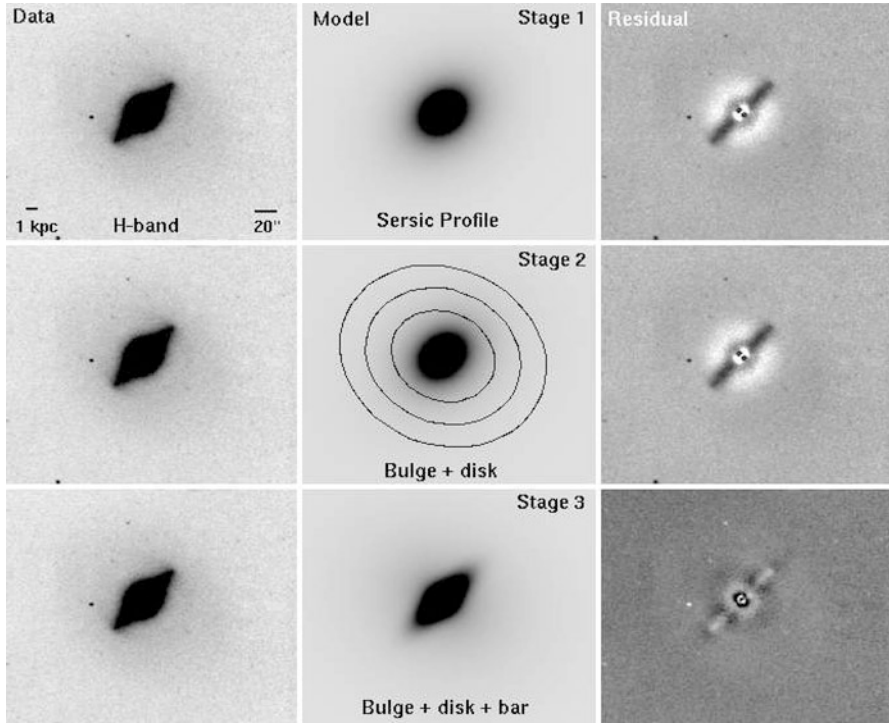


Fig. 2.5 Complete 2D decomposition for NGC 4643. Note the prominent bar residuals in the residual for the Stage 1 and Stage 2 bulge-disk decomposition. This is a case where the prominent bar causes the Stage 2 bulge-disk fit to artificially extend the bulge and inflate the B/T . The disk fitted in Stage 2 has a low surface brightness and is very extended, well beyond the real disk: the b/a and PA of the fitted disk is shown as contours. Stage 3 bulge-disk-bar decomposition provides the best model. The χ^2 for the Stage 1, Stage 2, and Stage 3 residual images are 7,360.7, 7,284.8, and 2,111.59, respectively. See Table 2.3 for the fit parameters

1. GALFIT calculates a χ^2 and χ^2_v for each model. It was found that χ^2 almost universally declines between the Stage 2 and Stage 3 fits for a given object. This is because in the Stage 3 fit, five extra free parameters (bar luminosity, r_e , Sérsic index, b/a , and PA) are added with the Sérsic bar component, allowing GALFIT to almost always make a lower χ^2 model during Stage 3. However, this does not necessarily mean that the solution in Stage 3 is more correct physically. Thus, an increasing χ^2 was interpreted as a sign that the Stage 3 fit should not be adopted, but a decreasing χ^2 was not considered as a sufficient condition to adopt Stage 3.
2. In cases with prominent bars, a symmetric light distribution due to unsubtracted bar light was often found in the Stage 1 and Stage 2 bulge-disk residuals. This was strong evidence that the Stage 3 bulge-disk-bar fit be selected. NGC 4643 is shown in Fig. 2.5 because it has a particularly striking bar residual; the corresponding fit parameters appear in Table 2.3. Note that in all figures and tables, we adopt the convention that PA values are positive/negative if they are measured from North counterclockwise/clockwise.

Table 2.3 Decomposition For NGC 4643

Fit		r_e or h (")	r_e or h (kpc)	n	b/a	Position angle	Fractional light (%)
(1)	(2)	(3)	(4)	(5)	(6)	(7)	(8)
Stage 1	Sérsic	27.90	2.66	4.44	0.80	-51.03	100
Stage 2	Bulge	23.86	2.30	4.16	0.80	-51.08	34.6
	Disk	335.88	32.33	1.00	0.84	66.94	65.4
Stage 3	Bulge	5.43	0.52	2.53	0.90	60.52	25.0
	Disk	48.22	4.64	1.00	0.84	66.94	54.1
	Bar	21.30	2.05	0.62	0.37	-45.84	20.9

Columns are: (1) Indicates whether the model is for Stage 1 (pure Sérsic profile), Stage 2 (bulge+disk or bar+disk), or Stage 3 (bulge+disk+bar). (2) One of pure Sérsic profile, Sérsic bulge, exponential disk, or Sérsic bar. (3) Effective radius of the bulge/bar or disk scalelength in arcseconds. (4) Effective radius of the bulge/bar or disk scalelength in kpc. (5) The Sérsic index of the profile. (6) Axis ratio of the component. (7) Position angle in degrees of the component. Positive angles are East of North. (8) The percentage of total galaxy light contributed by the component

3. The Stage 2 and Stage 3 models were selected only so long as the model parameters were all well behaved. In unbarred galaxies, the Stage 3 model parameters might be unphysically large or small, in which case the Stage 2 fit was favored. Conversely, in galaxies with prominent bars, the bulge component of the Stage 2 bulge-disk fit tends to grow too extended in size. Addition of a bar in the Stage 3 bulge-disk-bar fit removes this artifact, giving a more physical solution. An extreme example of this situation is the barred galaxy NGC 4548, which has a prominent bar and a faint disk. The Stage 2 fit, based on a Sérsic bulge and exponential disk, is highly inadequate to describe the bulge, disk, *and* the bar because it leads to an extremely extended bulge. The Stage 3 bulge-disk-bar fit, however, yields a believable fit with a prominent bar. The results of Stage 1, Stage 2, and Stage 3 are displayed in Fig. 2.6 and Table 2.4.
4. Not all barred galaxies had unphysical Stage 2 models. Instead, the bulge could be stretched along the *PA* of the bar, giving the bulge a lower Sérsic index and larger effective radius. A Stage 3 model that returned the bulge to a size and shape more representative of the input image was favored over the Stage 2 fit. Figure 2.7 and Table 2.5 demonstrate this behavior in NGC 4902. We distinguish this effect from cases like NGC 4548 (Fig. 2.6 and Table 2.4) where the Stage 2 fit is completely wrong.
5. In cases where there was no bar, GALFIT can sometimes be enticed into fitting a bar to any existing spiral arms, rings, or the clumpy disks of late-type spirals. Stage 3 fits in these cases could be discarded by noting the resulting discrepancies in appearance between the galaxy images and the Stage 3 model images. Examples of false bars are shown in Fig. 2.8.

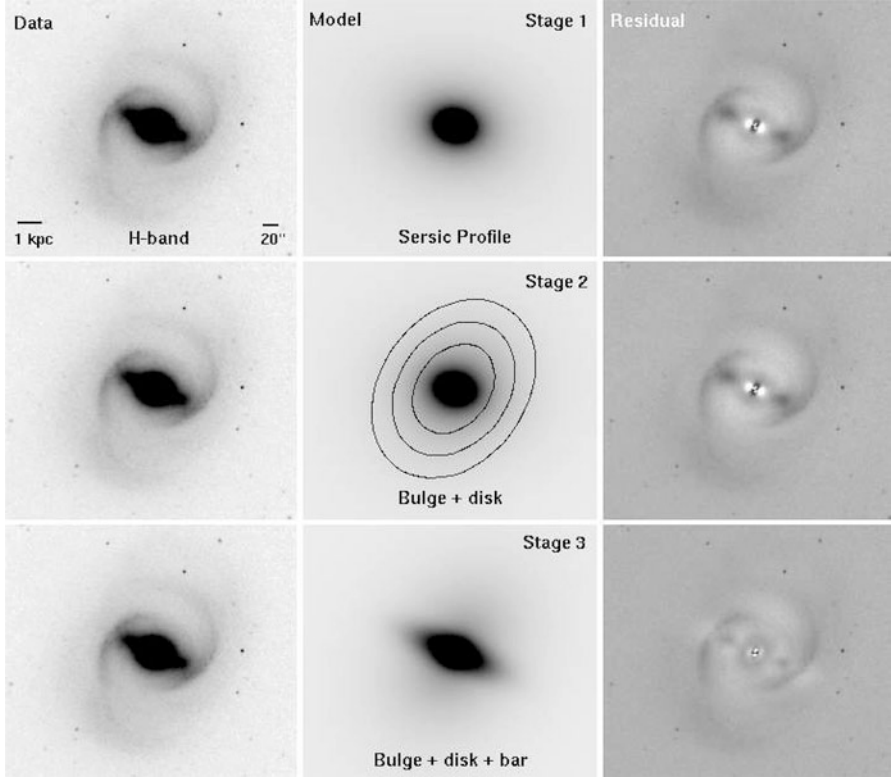


Fig. 2.6 The complete 2D decomposition for NGC 4548. This is an extreme example where the prominent bar results in an extended bulge and inflated B/T in the Stage 2 bulge-disk fit. Like NGC 4643 in Fig. 2.5, the disk fitted in Stage 2 has a low surface brightness and is very extended: its b/a and PA are shown as contours. Stage 3 bulge-disk-bar decomposition provides the best model. The χ^2_{ν} for the Stage 1, Stage 2, and Stage 3 residual images are 7,076.1, 6,301.3, and 3,260.4, respectively. See Table 2.4 for the fit parameters

After fitting the whole sample and picking the best fit from either the Stage 2 bulge-disk decomposition or the Stage 3 bulge-disk-bar decomposition, we also performed the following extra tests. For our sample S1 of 143 bright ($M_B \leq -19.3$) low-to-moderately inclined ($i \leq 70^\circ$) spirals in the OSUBSGS survey, we determine the fraction (75 of 143 or $\sim 52\%$) of spiral galaxies where a bulge-disk-bar decomposition was picked as the best fit for the H -band image. There are also eight galaxies with pure bar-disk fits. The H -band bar fraction, which is defined as the fraction of disk galaxies that are barred, is therefore $58.0 \pm 4.13\%$ (83 of 143). We then compared our results ($58.0 \pm 4.13\%$) with the H -band bar fraction (60%) determined from ellipse fits of the OSUBSGS sample by MJ07, with a slightly more conservative inclination cut ($i \leq 60^\circ$). The two numbers are in excellent agreement. As a further check to our fits, we compare the bar and unbarred classification for individual galaxies from our fits with those from MJ07, which were based on ellipse

Table 2.4 Decomposition For NGC 4548

Fit		r_e or h (")	r_e or h (kpc)	n	b/a	Position angle	Fractional light (%)
(1)	(2)	(3)	(4)	(5)	(6)	(7)	(8)
Stage 1	Sérsic	154.59	5.19	5.19	0.80	78.31	100
Stage 2	Bulge	57.86	1.94	4.32	0.76	75.77	61.5
	Disk	60.39	2.03	1.00	0.75	-32.54	38.5
Stage 3	Bulge	6.98	0.23	1.56	0.88	-66.50	13.0
	Disk	58.22	1.96	1.00	0.75	-32.54	68.6
	Bar	44.91	1.51	0.51	0.35	66.65	18.4

Columns are: (1) Indicates whether the model is for Stage 1 (pure Sérsic profile), Stage 2 (bulge+disk or bar+disk), or Stage 3 (bulge+disk+bar). (2) One of pure Sérsic profile, Sérsic bulge, exponential disk, or Sérsic bar. (3) Effective radius of the bulge/bar or disk scalelength in arcseconds. (4) Effective radius of the bulge/bar or disk scalelength in kpc. (5) The Sérsic index of the profile. (6) Axis ratio of the component. (7) Position angle in degrees of the component. Positive angles are East of North. (8) The percentage of total galaxy light contributed by the component

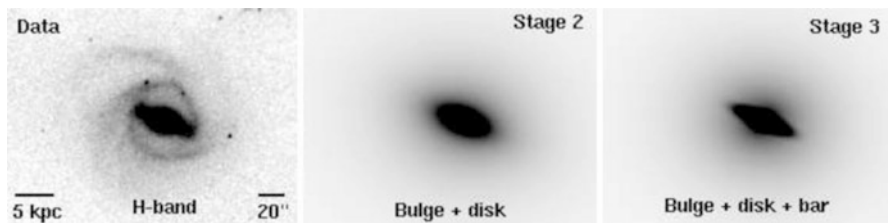


Fig. 2.7 This plot shows the data image, Stage 2 model, and Stage 3 model for NGC 4902. The Stage 2 bulge is too bright and is extended along the major axis of the bar ($B/T=31.2\%$ and $b/a=0.45$). In Stage 3, the bulge and bar are fit with distinct components ($B/T=5.59\%$, bulge $b/a=0.68$, Bar/ $T=9.97\%$, bar $b/a=0.22$). All other fit parameters appear in Table 2.5

fits. Of the 73 galaxies that we classify as barred, and that are mutually fitted by MJ07, 54 (74%) are also classified as barred by MJ07. The remaining 19 (26%) galaxies are mainly weakly barred (with Bar/ T below 0.08). Their RC3 optical types are weakly barred AB (10), barred B (7), and unbarred A (2).

In most previous bulge-disk and bulge-disk-bar 2D decomposition, the issue of parameter coupling and the systematic exploration of local versus global minima in χ^2 have been ignored. Quantifying how the parameters are coupled is important in measuring error bars for the model parameters. With 2D models containing several free parameters, this is not an easy task. Although we also do not address this problem in rigorous detail, we describe in Sect. 2.4.4 simple test that explores parameter coupling in our models.

Table 2.5 Decomposition For NGC 4902

Fit (1)		r_e or h ($''$) (3)	r_e or h (kpc) (4)	n (5)	b/a (6)	Position angle (7)	Fractional light (%) (8)
Stage 1	Sérsic	154.4	28.8	5.11	0.54	69.0	100
Stage 2	Bulge	11.5	2.15	1.02	0.38	68.5	17.4
	Disk	32.8	6.12	1.00	0.84	81.1	82.6
Stage 3	Bulge	4.31	0.80	0.85	0.68	-52.96	5.59
	Disk	29.2	5.45	1.00	0.84	81.1	82.6
	Bar	14.1	2.64	0.39	0.22	66.37	9.97

Columns are: (1) Indicates whether the model is for Stage 1 (pure Sérsic profile), Stage 2 (bulge+disk or bar+disk), or Stage 3 (bulge+disk+bar). (2) One of pure Sérsic profile, Sérsic bulge, exponential disk, or Sérsic bar. (3) Effective radius of the bulge/bar or disk scalelength in arcseconds. (4) Effective radius of the bulge/bar or disk scalelength in kpc. (5) The Sérsic index of the profile. (6) Axis ratio of the component. (7) Position angle in degrees of the component. Positive angles are East of North. (8) The percentage of total galaxy light contributed by the component

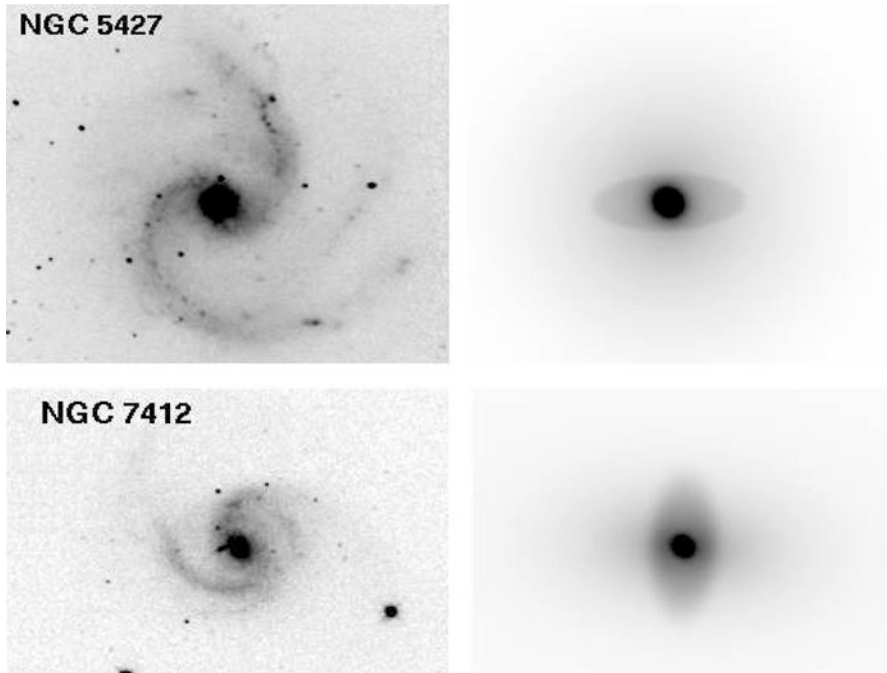


Fig. 2.8 The data images and Stage 3 bulge-disk-bar decomposition models of NGC 5427 and NGC 7412 are shown. The Stage 3 models each distinctly show a false bar component, which is not present in the data images. The false components can be inspired by prominent spiral arms, such as those present in these galaxies. Such cases are flagged during the visual inspection of fits and the Stage 3 bulge-disk-bar decomposition is discarded in favor of the Stage 2 bulge-disk decomposition

2.4 Extra Tests to Verify Correctness of Fits

2.4.1 Varying b/a as a Function of Radius

Models generated with GALFIT do not allow the b/a of the bulge, disk, or bar to vary with radius. Since real bulges may have a varying b/a , it is legitimate to investigate the impact of fixing the bulge b/a on the estimated B/T . We therefore performed the following test on NGC 4548. To mimic a model bulge of varying b/a , we fitted the bulge light of NGC 4548 with ten concentric Sérsic profiles of increasing r_e and varying b/a . The r_e of the outermost profile comes from the original bulge model (see Table 2.4) where b/a was kept constant with radius. The separation in r_e between adjacent profiles is 0.5 pixels (0.75"). The luminosity, Sérsic index, b/a , and PA of each profile were free parameters. The disk and bar components were fixed to the values in Table 2.4, as the emphasis was on the change in the bulge.

Figure 2.9 compares the B/T obtained by fitting the bulge of NGC 4548 with a Sérsic model of constant b/a as opposed to a Sérsic model varying b/a . The bulge b/a (0.88), PA (-66.5°), and B/T (13 %) from the original Sérsic fit of constant b/a (Table 2.4) are indicated with horizontal lines on the three panels. The top two panels show the run of b/a (0.85 to 1.0) and PA (-90° to $+90^\circ$) of the ten concentric Sérsic profiles. It can be seen that the Sérsic indices of the ten bulge models were generally higher toward the center and declined at larger r_e , indicating that the fitted bulge is more concentrated at the center. The bottom panel shows the cumulative B/T calculated by summing all models with $r \leq r_e$. The last point representing the summed B/T from all ten components is 14.5 %, in good agreement with the 13.0 % value from the Sérsic fit of constant b/a . Thus, using a Sérsic model of constant b/a , does not have any significant adverse impact on our derived B/T in NGC 4548.

2.4.2 Fitting Artificially Simulated Images

An elementary test is to determine if GALFIT can recover the known parameters of artificially simulated noisy images. The images were simulated by taking parametric model images produced by GALFIT, and adding noise to the images with the PyFITS module for Python (Barrett and Bridgman 1999). Noise in each pixel was calculated by adding in quadrature the noise due to the source, sky, and read noise. The standard deviation of pixel noise in electrons was computed as

$$\sigma = \sqrt{T_{source} + T_{sky} + T_{read}^2}, \quad (2.5)$$

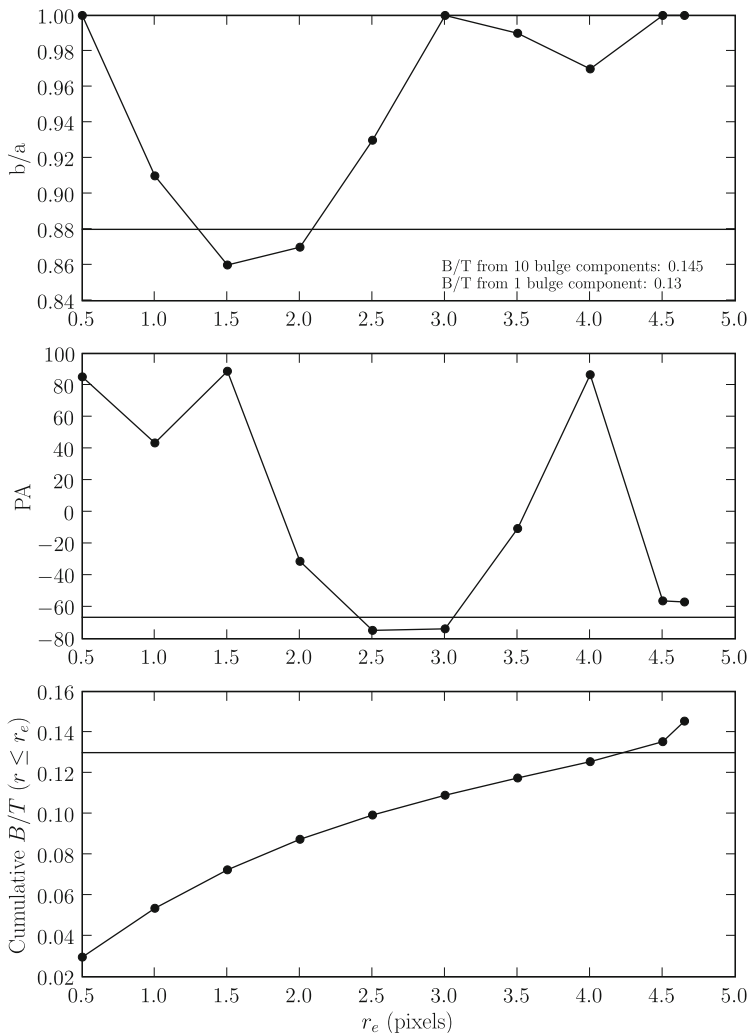


Fig. 2.9 This plot compares the B/T obtained by fitting the bulge of NGC 4548 with a Sérsic model of constant b/a as opposed to a Sérsic model varying b/a . To mimic a Sérsic model with varying b/a in GALFIT, the bulge was fitted with ten concentric Sérsic profiles with fixed r_e , each separated by $0.75''$. The *top two panels* show the run of b/a and PA of the ten concentric Sérsic profiles. The *bottom panel* shows the cumulative B/T calculated by summing all models with $r \leq r_e$. The bulge b/a (0.88), PA (-66.5), and B/T (13%) from the original Sérsic fit of constant b/a (Table 2.4) are indicated with *horizontal lines* on the three panels

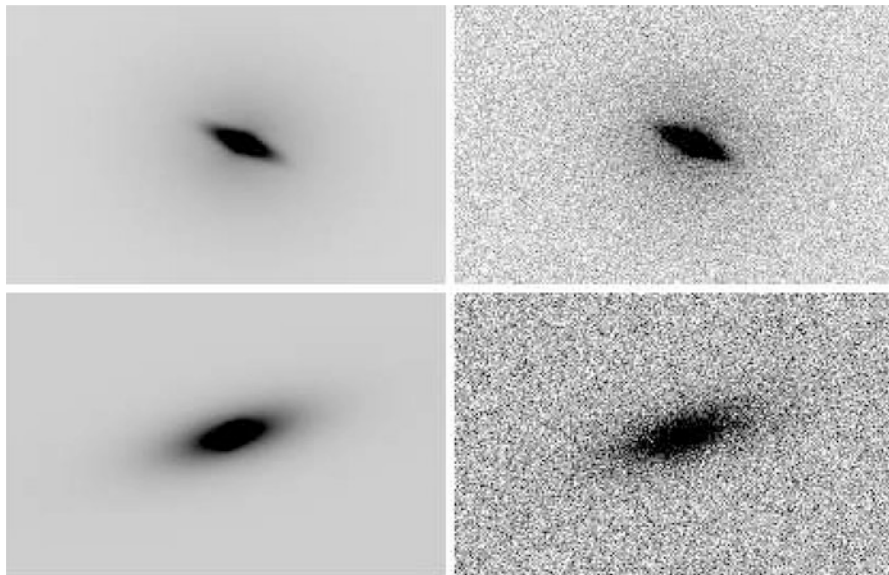


Fig. 2.10 An elementary test is to determine if GALFIT can recover the known parameters of artificial noisy images. Noisy images were simulated by taking parametric model images (*left panels*) produced by GALFIT, and adding noise and sky background (*right panels*). The noisy images were then fitted to see if the original known parameters can be recovered. See Sect. 2.4.2 for details

where T_{source} is the number of electrons due to the source, T_{sky} is the number of electrons due to the sky, and T_{read} is the detector read noise. The contribution due to detector dark current was very small and therefore neglected. The offset added to each pixel was drawn from a normal distribution centered at zero with standard deviation σ .

Our test sample consisted of 40 models (20 bulge-disk and 20 bulge-disk-bar) with noise added as described. Thirty of the images included point sources as extra components. The range explored for each parameter in the model images is a fair representation of the parameter space covered by our full sample (e.g., B/T ranges from 0.02 to 0.70, the bulge index ranges from ~ 0 –5, and the full range of possible bulge and bar PA was also tested (-90° to $+90^\circ$)). In terms of surface brightness, the models span five magnitudes in mean surface brightness inside the disk scalelength. Examples of the noise-added models are shown in Fig. 2.10.

The noisy images were subjected to the 2D decomposition procedure outlined in Fig. 2.4. GALFIT reproduced the model (bulge, disk, bar, and point source) parameters quite closely for the majority of the test cases. Figure 2.11 compares the recovered versus original model parameters. Except for some extreme cases where the images were highly distorted by noise, all parameters were recovered to within a few percent. Figure 2.12 plots the ratio of model-to-recovered parameter against mean surface brightness inside the disk scalelength; there is no strong trend in error

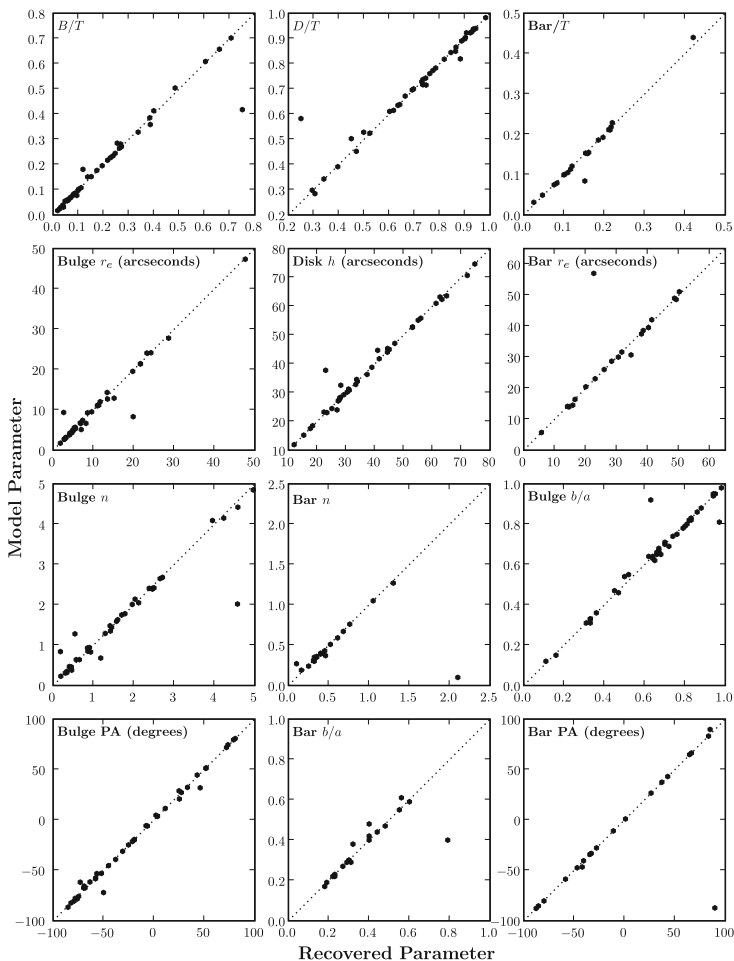


Fig. 2.11 The plots compare recovered versus original model parameters for the simulated images discussed in Sect. 2.4.2. The vertical axis limits demonstrate the range explored for each parameter. The *dotted line* shows $y = x$ for comparison. Except for some extreme cases where the images were highly distorted by noise, all parameters were recovered to within a few percent

with dimming surface brightness. This suggests our decompositions are effective across the parameter space spanned by our sample. The overall success of this test is evidence that GALFIT is able to converge to the absolute minimum in χ^2 space for our bulge-disk and bulge-disk-bar decompositions when the input is the sum of parametric functions.

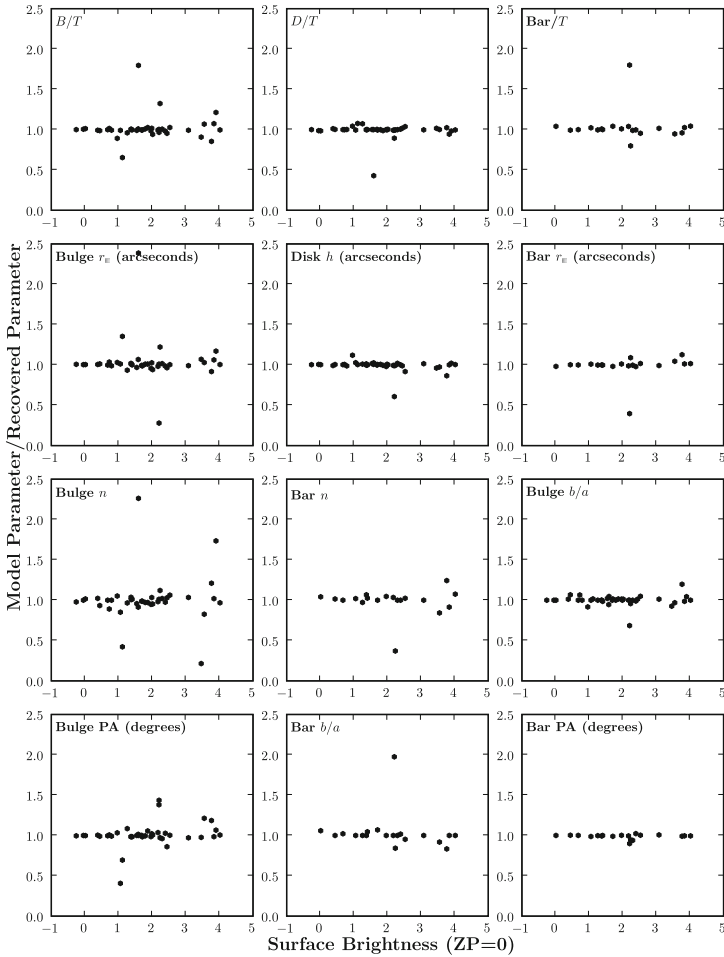


Fig. 2.12 The ratio of model-to-recovered parameter is plotted against mean surface brightness inside the disk scalelength, $\mu = mag + 2.5 \times \log_{10}(2 \times \pi \times b/a \times h^2)$, for the simulated images discussed in Sect. 2.4.2. Surface brightness is not photometrically calibrated and is shown for a zeropoint of 0

2.4.3 Using 1D Decomposition To Generate Guesses for Bulge Parameters

It is important to verify that GALFIT converges to the same solution even if the initial guesses for the bulge parameters in Stage 2 and 3 are different. Bulge-disk decomposition from 1D profiles provides an alternative means of generating initial guesses. While 1D bulge-disk decompositions of radial profiles along the bar major axis can be influenced by the bar, decomposition of cuts along the bar minor axis

Table 2.6 Checking GALFIT robustness with different input guesses for Stage 3

(1)	B/T (%)	Bulge r_e (")	Bulge n	D/T (%)	Disk h (")	Bar/ T (%)	Bar r_e (")	Bar n (9)
	(2)	(3)	(4)	(5)	(6)	(7)	(8)	(9)
NGC 4548								
Initial guesses from 1D decomposition	17.5	7.39	1.17	63.5	28.4	19.0	37.5	0.54
Stage 3 output	13.0	6.98	1.56	68.6	58.2	18.4	44.9	0.51
Initial guesses from Stage 2	11.1	7.50	1.70	69.9	64.5	19.1	37.5	0.54
Stage 3 output	13.0	6.98	1.56	68.6	58.2	18.4	44.9	0.51
NGC 4643								
Initial guesses from 1D decomposition	33.6	7.18	0.86	40.4	37.5	26.0	22.0	0.60
Stage 3 output	25.0	5.43	2.53	54.1	48.2	20.9	21.3	0.62
Initial guesses from Stage 2	24.1	5.30	2.5	51.8	46.4	24.1	22.0	0.60
Stage 3 output	25.0	5.43	2.53	54.1	48.2	20.9	21.3	0.62

For each galaxy, the rows are: (1) The initial guesses to Stage 3 provided by 1D decomposition. (2) The corresponding output for the input of row (1). (3) The initial guesses to Stage 3 provided by Stage 2. (4) The corresponding output for the input of row (3)

The columns are: (2) Bulge-to-total luminosity fraction. (3) Effective radius of the bulge in arcseconds. (4) The Sérsic index of the profile. (5) Disk-to-total luminosity fraction. (6) Disk scalelength in arcseconds. (7) Bar-to-total luminosity fraction. (8) Bar effective radius in arcseconds. (9) Bar Sérsic index

will not be influenced as heavily. The resulting bulge and disk parameters should be adequate guesses for Stage 3 of our 2D decomposition method.

We tested the robustness of our Stage 3 fits by extracting initial guesses for the bulge and disk using 1D decomposition along the bar minor axis. The nonlinear least-squares algorithm designed to perform the 1D decomposition simultaneously fits the sky-subtracted profiles with the sum of a Sérsic bulge and an exponential disk, while ignoring the PSF. The results from the 1D decomposition include a bulge magnitude, r_e , Sérsic index, disk magnitude, and disk scalelength.

The robustness of several bulge-disk-bar fits were tested by using the results of the 1D decomposition as input to Stage 3. The 1D decompositions do not provide information about the axis ratio (b/a) or PA , so these parameters for the bulge were estimated by eye; for the disk, the b/a and PA were fixed to the values determined by ellipse fitting, as described in Sect. 2.3.2. The initial bar parameters were unchanged from the earlier Stage 3 fits. In all cases, the new models were identical to the Stage 3 models. As an example, Table 2.6 compares Stage 3 input derived from 1D decomposition and GALFIT for NGC 4548 and NGC 4643. In each case, both sets of input reproduced the same results.

2.4.4 Parameter Coupling

Assessing the coupling between model parameters is complicated when models have a large number of free parameters. A standard approach is to calculate confidence regions using multi-dimensional ellipsoids for a given $\Delta\chi^2$ contour. As the errors in the GALFIT models are not normally distributed, but are instead dominated by the systematics of galaxy structure, this approach does not yield meaningful results because of the ambiguity in assessing which $\Delta\chi^2$ contour levels are statistically significant.

We carry out a simple test for representative galaxies to determine not only the effects of parameter coupling, but also the effect parameter coupling has on model parameter errors, paying particularly close attention to B/T , D/T , and Bar/T , as they are of primary interest. We perform this test on four representative galaxies (NGC 3885, NGC 4151, NGC 4643, and NGC 7213). Two are barred (NGC 4151 and NGC 4643). Two have high ($n > 2$) bulge indices (NGC 4643 and NGC 7213), and the other two have low ($n < 2$) bulge indices.

We fit two and three-component bulge-disk and bulge-disk-bar models using fixed bulge indices of $n = 1$ and $n = 4$. The initial inputs to these fits were the same as those used to generate the model in which bulge n is a free parameter. We then had GALFIT re-fit the models with bulge index as a free parameter using these output model parameters as input initial guesses. We compare the output of these two fits with the best fit as selected in Sect. 2.3.3, in which bulge n is a free parameter. Ideally, the re-fits should converge to the same final parameters as the selected best fit.

Table 2.7 displays the outcome of this test for the four representative systems. For barred galaxies NGC 4643 and NGC 4151, the $n = 1$ and $n = 4$ re-fits converged to the same χ^2 as when bulge n is initially left a free parameter. B/T , D/T , and Bar/T are precisely equal for NGC 4643, while for NGC 4151 there is a small dispersion of 0.1–0.2%. For unbarred galaxies NGC 3885 and NGC 7213, the $n = 1$ re-fits again converged to the same χ^2 and model parameters as when bulge n is initially left a free parameter. This is not true for the $n = 4$ re-fits. When the $n = 4$ condition is enforced, the bulges in these cases become too extended and luminous while the χ^2 drop below those when bulge n is initially left a free parameter. During the $n = 4$ re-fits, B/T increases further at the expense of D/T and the χ^2 remain unchanged or decrease further. The B/D ratio from the $n = 4$ re-fit for NGC 3885 is 1.3, roughly 3.5 times higher than when n is free. Given that NGC 3885 is an S0/a galaxy with a bulge embedded in a smooth extended disk, the latter B/D is arguably too large. For NGC 7213, the $n = 4$ re-fit yields starkly unphysical values. The B/D ratio is 11.3, and r_e/h , the ratio between bulge effective radius and disk scalelength is 9.0. The lower χ^2 in these cases cannot be taken seriously as the bulges are too luminous and the resulting B/D ratios do not match the data images.

As illustrated by the above discussion and Table 2.7, this test shows that in some cases (e.g., NGC 4643 and NGC 4151) GALFIT converges to the similar model parameters and B/T , D/T , and Bar/T while starting from highly different

Table 2.7 Parameter coupling

Type of fit	χ^2	Bulge r_e	Bulge n	B/T	Disk h	D/T	Bar r_e	Bar n	Bar/ T
(1)	(2)	(3)	(4)	(5)	(6)	(7)	(8)	(9)	(10)
NGC 3885									
initial input	11,241.33	2.32	2.00	27.7	10.44	72.3	—	—	—
n=free	8,210.12	3.13	0.46	27.1	11.94	72.9	—	—	—
n=1 fixed	[8,307.82]	[2.96]	[1.00]	[29.1]	[12.90]	[70.9]	—	—	—
n=4 fixed	[7,373.55]	[6.28]	[4.00]	[53.7]	[20.45]	[46.3]	—	—	—
n=1 re-fit	8,210.12	3.13	0.46	27.1	11.94	72.9	—	—	—
n=4 re-fit	7,258.46	7.11	4.49	57.3	19.87	42.7	—	—	—
NGC 7213									
initial input	605,757.39	5.80	4.00	56.4	9.25	43.6	—	—	—
n=free	71,170.10	19.55	2.68	65.7	63.19	34.3	—	—	—
n=1 fixed	[96,312.29]	[7.81]	[1.00]	[31.4]	[27.79]	[68.6]	—	—	—
n=4 fixed	[70,998.69]	[41.11]	[4.00]	[95.4]	[6.75]	[4.6]	—	—	—
n=1 re-fit	71,170.10	19.53	2.68	65.7	63.16	34.3	—	—	—
n=4 re-fit	69,970.51	72.04	5.60	91.9	7.98	8.1	—	—	—
NGC 4643									
initial input	7,841.46	5.34	2.50	24.1	46.40	51.8	22.04	0.60	24.1
n=free	2,111.59	5.43	2.53	25.0	48.22	54.1	21.30	0.62	20.9
n=1 fixed	[3,001.98]	[2.31]	[1.00]	[9.6]	[53.37]	[57.0]	[15.05]	[0.88]	[33.4]
n=4 fixed	[2,491.06]	[12.08]	[4.00]	[35.4]	[87.22]	[51.7]	[23.37]	[0.61]	[12.9]
n=1 re-fit	2,111.59	5.43	2.53	25.0	48.21	54.1	21.30	0.62	20.9
n=4 re-fit	2,111.59	5.43	2.53	25.0	48.22	54.1	21.30	0.62	20.9
NGC 4151									
initial input	1,388,891.11	7.50	0.50	24.6	33.00	65.0	55.50	0.10	10.3
n=free	16,391.66	9.36	0.44	41.3	37.74	50.3	57.00	0.10	8.4
n=1 fixed	[18,100.67]	[11.58]	[1.00]	[42.2]	[86.28]	[41.1]	[56.70]	[0.17]	[16.7]
n=4 fixed	[20,051.12]	[108.39]	[4.00]	[51.4]	[8.21]	[20.4]	[68.23]	[0.28]	[28.2]
n=1 re-fit	16,391.58	9.38	0.44	41.2	38.31	49.7	55.57	0.12	9.0
n=4 re-fit	16,390.93	9.36	0.44	41.3	38.20	49.8	55.88	0.11	8.8

For each galaxy, the rows are: (1) The model outputs (columns 2 to 10) from GALFIT based on the Stage 1 or Stage 2 fits. These outputs are used as initial guesses in the fits for rows 2 and 3. (2) The model outputs (columns 2 to 10) from GALFIT when the bulge n is allowed to vary freely, and the input guesses are based on the parameters in columns 2 to 10 of row 1. (3) The model outputs (columns 2 to 10) from GALFIT when the bulge Sérsic index is held fixed at $n = 1$, and the input guesses are based on the parameters in columns 2 to 10 of row 1. The model is not always physically meaningful because the bulge index is fixed. (4) As in row 3, except that the bulge Sérsic index is now held fixed at $n = 4$. The model is not always physically meaningful because the bulge index is fixed. (5) The model outputs (columns 2 to 10) from GALFIT, when the bulge n is allowed to vary freely, but the input guesses are now based on the parameters in columns 2 to 10 of row 3. (6) The model outputs (columns 2 to 10) from GALFIT, when the bulge n is allowed to vary freely, but the input guesses are now based on the parameters in columns 2 to 10 of row 4. The columns are: (1) The type of fit whose model outputs are shown in columns 2 to 10. (2) The χ^2 of the fit. (3) Effective radius of the bulge in arcseconds. (4) The Sérsic index of the bulge (in the case of Stage 2 bulge-disk fits in row 1 and in the case of all fits in rows 2 to 6), or the Sérsic index of a single component (in the case of Stage 1 fits in row 1). (5) Bulge-to-total luminosity fraction. (6) Disk scalelength in arcseconds. (7) Disk-to-total luminosity fraction. (8) Bar effective radius in arcseconds. (9) Bar Sérsic index. (10) Bar-to-total luminosity fraction

initial input guesses (e.g., bulge $n = 1$, bulge $n = 4$, and bulge n based on the Stage 2 fits) in different regions of parameter space. For NGC 3885 and NGC 7213, however, during the $n = 4$ re-fits GALFIT converged to models that were unphysical and different compared with the reasonable models generated with input guesses corresponding to the bulge fixed at $n = 1$ or the bulge n based on output from Stage 1. In effect, when the initial input guesses were very different from the data images, the resulting models were found, in spite of the lower χ^2 , to be unphysical through comparison with the input data images. We emphasize that for all sources analyzed in the paper, the data, converged model output, and residuals are always inspected before adopting the best final fit (see Sect. 2.3.3).

Table 2.7 also provides hints as to how the model parameters are coupled to bulge index. As suggested in the above discussion, fixing the bulge index to $n = 4$ leads to a more extended and luminous bulge, causing bulge r_e and B/T to rise without fail for increasing bulge index. The disk is coupled with the bulge such that increasing bulge index, bulge r_e , and B/T yields a reduction in D/T . At the same time, disk scalelength either increases (NGC 3885 and NGC 4643) or decreases (NGC 3885 and NGC 4151); in the latter two cases, the disk becomes very compact and the bulge quite extended. The behavior of the bar is coupled with *both* the bulge and disk. In the case of NGC 4643, as bulge index is raised to $n = 4$, bar r_e becomes slightly larger, but Bar/T falls by a factor of 2.6 as light is redistributed from the bar and disk to the bulge. Bar index also declines as the bar assumes a flatter profile. For NGC 4151, bar r_e again increases slightly, but this time Bar/T rises by a factor of 1.7 as light is transferred from the disk to the bulge and bar.

Based on the above test, we stress that GALFIT was able to overcome this parameter coupling in the cases where the input guess parameters well-reflected the data images.

2.5 Results and Discussion

2.5.1 Impact of Bars in 2D Decomposition

From the Stage 2 bulge-disk decomposition and Stage 3 bulge-disk-bar decompositions, which we performed on all objects (Sect. 2.3.2) we saw firsthand the effects of adding a bar to the fit of a barred galaxy. We summarize below some of these effects in order to underscore the importance of including a bar component in the 2D luminosity decomposition of barred galaxies

1. During the Stage 2 bulge-disk decomposition of a barred galaxy, the luminosity which comes from the galaxy's disk, bulge, and bar gets distributed only between two model components: the model bulge and disk. Since the disk b/a and PA are measured independently and held constant during the fits, the Stage 2 model tends to distort the bulge in order to fit the bar. Thus, the bulge in the Stage 2 bulge-disk decomposition of a barred galaxy can be artificially long or

too bright and extended. When a model bar component is added in the Stage 3 bulge-disk-bar decomposition of a barred galaxy, it forces a reshuffling of the luminosity between the three components. Generally, the bulge declines in luminosity, whereas light can be either taken from, or added back, to the disk.

2. We find that the inclusion of a bar component in the Stage 3 bulge-disk-bar decomposition of a barred galaxy reduces the bulge fractional luminosity B/T , compared with the Stage 2 bulge-disk decomposition. For our 75 barred galaxies, the reductions correspond to factors of less than two, 2 to 4, and above 4, in 36, 25, and 39 % of barred galaxies, respectively. The larger changes in B/T occur in very strongly barred galaxies, where a prominent bar cause the Stage 2 bulge-disk decomposition to overestimate the bulge. For instance, B/T declines in both of NGC 4643 (Fig. 2.5 and Table 2.3) and NGC 4548 (Fig. 2.6 and Table 2.4). In the latter case, B/T is reduced by a factor of ~ 5 between Stage 2 and Stage 3. These examples underscore the importance of including bars in 2D luminosity decomposition of very strongly barred galaxies.
3. The scalelength of the disk is generally unchanged by including the bar. NGC 4548 (Fig. 2.6 and Table 2.4) is a good example. Sometimes, however, the disk from the Stage 2 bulge-disk decomposition of a barred galaxy is erroneous due to a poor fit. The disk parameters from the Stage 3 bulge-disk-bar decomposition are quite different in such cases. NGC 4643 (Fig. 2.5 and Table 2.3) illustrates this behavior.

We find that for our sample S1 of 143 bright ($M_B \leq -19.3$) low-to-moderately inclined ($i \leq 70^\circ$) spirals (Fig. 2.1) in the OSUBSGS survey, 75 of 143 or $\sim 52\%$ are better fit with a Stage 3 bulge-disk-bar decomposition than a Stage 2 bulge-disk decomposition. There are also eight galaxies with pure bar-disk fits. As stated in Sect. 2.3.3, the resulting H -band bar fraction ($58.0 \pm 4.13\%$ or 83 of 143) is in excellent agreement with the H -band bar fraction of 60 % reported by MJ07 based on ellipse fits of the OSUBSGS sample, with a slightly more conservative inclination cut ($i \leq 60^\circ$).

2.5.2 Mass in Bulges, Disks, and Bars

The fractional H -band luminosities in the bulge, disk, and bar (B/T , D/T , Bar/T) of each galaxy can be considered as a fractional mass if we assume that the same mass-to-light (M/L) ratio can be used to convert the H -band luminosities of both the numerator (B , D , or Bar) and the denominator (T) terms into a stellar mass. This is not an unreasonable assumption as the H -band M/L ratio is not very sensitive to differences in dust or age that might exist between the bulge, disk, and bar. The uncertainties in M/L can be estimated by looking at population synthesis models. Charlot et al. (1996) find that for idealized galaxies with a single generation of stars, the uncertainties in M/L ratio due to different input stellar models and spectra are roughly $\pm 35\%$ for a fixed metallicity and IMF. Furthermore, as the age of a stellar

Table 2.8 Mass breakdown of galactic structures

Structure	Mass
Bulges	$18.9 \pm 3.49 \%$
Disks	$71.6 \pm 4.02 \%$
Bars	$9.58 \pm 2.62 \%$
Bulges with $n > 2$	$10.4 \pm 2.72 \%$
Bulges with $n \leq 2$	$8.42 \pm 2.47 \%$

population varies from ~ 0.5 to 10 Gyr, the K -band M/L ratio rises by a factor of ~ 2 to 3 (Charlot 1996). Asymptotic giant branch (AGB) stars dominate the NIR light for ages between 0.1 and 1 Gyr, while red giant branch (RGB) and super-giant branch (SGB) stars dominate between 1 and 10 Gyr.

In this paper, we convert the B/T light ratio determined from H -band images to a B/T mass ratio by assuming a constant mass-to-light (M/L) in the H -band for both the bulge and the rest of the galaxy. However, Moorthy and Holtzman (2006) present line strengths of bulges and inner disks for 38 spirals with Hubble types S0 to Sc. They show 76% of spirals have negative metallicity gradients. $B - K$ color gradients are shown to largely match metallicity gradients and are likewise negative outward, indicating bulge M/L is higher than in the disk and bar. If bulges are much older than the disks, then our prescription would underestimate the true B/T mass ratio. If we assume an extreme case where bulges are ~ 12 Gyr and the disk light is dominated by a young 3 Gyr population, our assumption of a constant H -band M/L ratio would underestimate the true B/T by a factor of ≤ 2 (Charlot 1996). In several sections of the paper (e.g., Sects. 2.5.3 and 2.5.8), we illustrate how our main results would change if the true B/T was higher by up to a factor of two. On the other hand, central regions of galaxies may harbor intense episodes of star formation. If the bulge is younger than the disk and happens to have star formation and a significant young population of massive stars, then our prescription could overestimate the true B/T mass ratio. This would make our current results on the high fraction of low B/T bulges even stronger.

Using the total galaxy stellar mass from Sect. 2.2.2, the fractional masses can be converted into absolute masses. (We do not convert the H -band luminosity directly into a mass as the H -band images do not have photometric calibration.) Using this procedure, the fractional masses in different components relative to the whole sample are presented in Table 2.8. For our sample S1 of 143 bright ($M_B \leq -19.3$) low-to-moderately inclined ($i \leq 70^\circ$) spirals with a mass-weighted mean Hubble type of Sab-Sb, we find that $\sim 70\%$ of the stellar mass is in disks, $\sim 10\%$ is in stellar bars and $\sim 20\%$ is in bulges (with $\sim 11\%$ in $n > 2$ bulges and $\sim 9\%$ in $n \leq 2$ bulges). Thus while bulges with $n \leq 2$ are highly ubiquitous (see next section), they only account for a small fraction of the total stellar mass budget.

Figure 2.13 shows the stellar mass for bulges, disks, and bars along the Hubble sequence.

It is useful to compare our results with those of Driver et al. (2006), who performed bulge-disk decomposition of B -band images with GIM2D on 10,095 galaxies from the Millennium Galaxy Catalog (Liske et al. 2003; Driver et al. 2005).

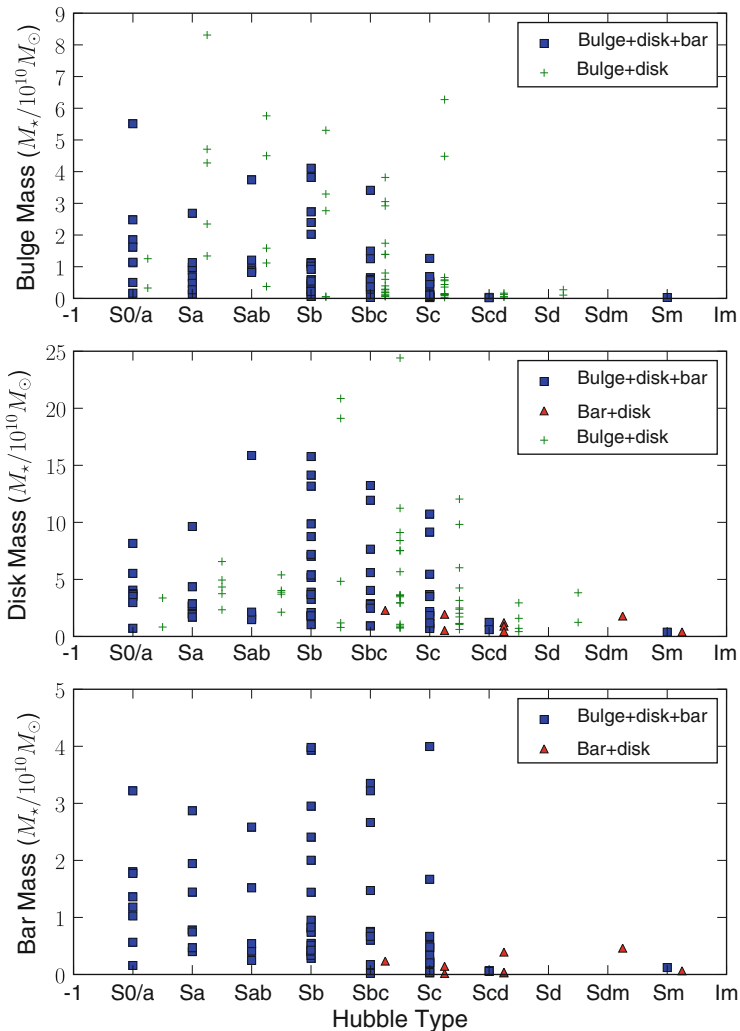


Fig. 2.13 The *top*, *middle*, and *bottom* panels show stellar mass for bulges, disks, and bars, respectively, along the Hubble sequence. Values are shown for sample S2 of 126 galaxies in Fig. 2.3. The legend in each panel indicates the type of decomposition used for each data point

They found 68.6% of the stellar mass to be in disks, and 32.6% in bulges (with 30.8% in high n bulges, and 1.8% in low $n \leq 2$ bulges). Their study thus finds a higher stellar mass fraction in all bulges (32.6% vs our 18.9%), and in high n bulges (30.8% vs our 10.4%), and a lower fraction in low $n \leq 2$ bulges (1.8% vs our 8.4%), and disks+bars (68.6% vs our 71.6% + 9.6%). This difference can be

attributed to the fact that the Driver et al. (2006) study did not perform bulge-disk-bar fits and thus, their B/T ratios may be skewed to higher values.

2.5.3 Distribution of Bulge Index and B/T

Figure 2.15 shows the individual and mean B/T and bulge Sérsic index, plotted, as a function of Hubble type and galaxy stellar mass. Barred and unbarred galaxies are shown separately. Figure 2.14 shows the relationship between bulge index and B/T .

We first consider the B/T values in Fig. 2.15. The mean B/T in barred galaxies is lower than in unbarred galaxies, but there is a large overlap in the individual values. The offset in the mean B/T of barred and unbarred galaxies reported here, agrees with the result of Laurikainen et al. (2007; see Sect. 2.5.4) on the same sample. We also note that B/T does not correlate with Bar/T (Fig. 2.16): aside from the six galaxies with large Bar/T (>0.3), most galaxies have low-to-moderate Bar/T and a wide range of B/T is seen at each Bar/T . This is reassuring and suggests that the bar fit is not arbitrarily biasing the B/T values. The distribution of Bar/T is further discussed in Sect. 2.5.5.

How does the B/T vary as a function of Hubble type and galaxy stellar mass? Bulges with very high B/T (>0.4) exist primarily in galaxies with high mass ($M_* > 6 \times 10^{10} M_\odot$) and early types (S0/a to Sab). Bulges with very low B/T (<0.1) lie primarily in lower mass galaxies with later morphologies (Sb to Sc). *It is striking that $\sim 69\%$ of bright ($M_B \leq -19.3$) low-to-moderately inclined ($i \leq 70^\circ$) spirals have $B/T \leq 0.2$: these bulges are pervasive and exist across the whole spectrum of S0/a to Sd.* The results are summarized in Table 2.9. We shall return to this point in Sect. 2.5.8. We note again that these B/T mass ratios were calculated assuming a constant M/L ratio in the H -band for the bulge and disk components. As noted in Sect. 2.5.2, if the bulge in these high mass spirals is much younger (older) than the disk and bar, then the B/T can be overestimated (underestimated) by up to a factor of two, and the limiting value of 0.2 for the B/T cited in the above fraction, would have to be modified in the extreme case to 0.1 and 0.4, respectively.

Some of the low $B/T \leq 0.2$ values for six barred S0/a and Sa galaxies in Fig. 2.15 may at first look suspicious. Balcells et al. (2007) report the mean B/T for S0 galaxies to be 0.25, so much smaller B/T are potentially worrisome. OSUBSGS H -band images of these objects in Fig. 2.17 show a smooth extended disk around the bulge. It should be noted that Hubble types were originally assigned on a combination of criteria including disk smoothness and spiral arm topology in addition to the prominence of the bulge. It is likely that these galaxies were assigned early Hubble types due to their smooth extended disks, in spite of their low bulge-to-disk ratio.

Similarly, some of the high $B/T \sim 0.4$ bulges in three of the Sc galaxies may at first seem odd. However, again, visual inspection of their image (Fig. 2.17) reveals prominent spiral arms and clumpiness, which may explain why they were assigned late Hubble types.

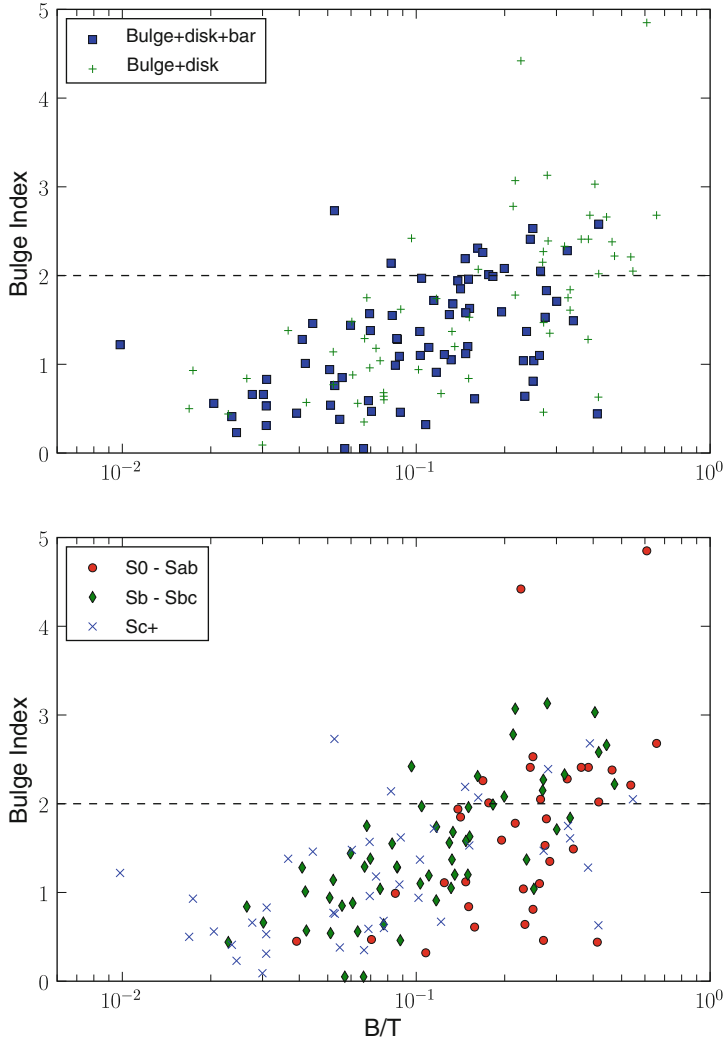


Fig. 2.14 The relation between B/T and bulge index is shown. In the *top panel*, galaxies are coded according to bar class. The legend indicates the type of decomposition used for each data point. In the *lower panel*, galaxies are coded according to Hubble type. A striking $\sim 76\%$ of bright spirals have low $n \leq 2$ bulges. Such bulges exist in barred and unbarred galaxies across a wide range of Hubble types, and their B/T range from 0.01 to 0.4, with most having $B/T \leq 0.2$. A moderate fraction ($\sim 22\%$) have intermediate $2 < n < 4$ bulges. These exist in barred and unbarred S0/a to Sd galaxies, and their B/T spans a wide range (0.05 to 0.5). Only ($\sim 1\%$) have $n \geq 4$

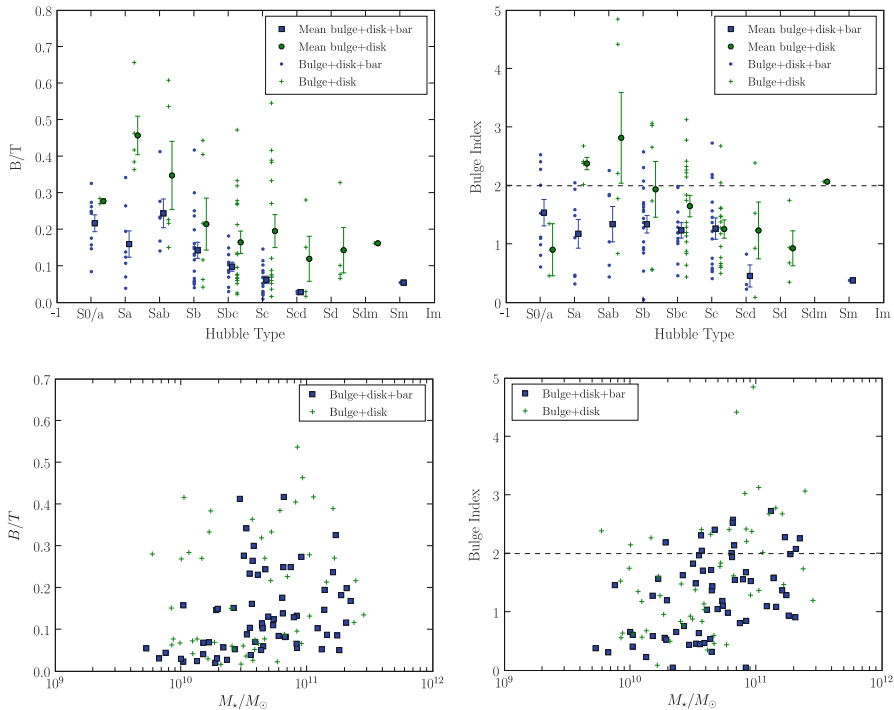


Fig. 2.15 The individual and mean B/T (*left panels*) and bulge Sérsic index (*right panels*) are plotted as a function of Hubble type for the sample S1 of bright galaxies, and as a function of galaxy stellar mass for sample S2. The error bars indicate the standard deviation of the population around the mean in each bin. The legend in each panel indicates the type of decomposition used for each data point. The mean B/T and bulge index in barred galaxies differ systematically from unbarred galaxies, but there is a large overlap in the individual values. As many as $\sim 69\%$ of bright spiral galaxies have $B/T \leq 0.2$; these bulges are pervasive and exist across the Hubble sequence. Furthermore, as many as $\sim 76\%$ of bright spirals have low $n \leq 2$ bulges. Such bulges exist in barred and unbarred galaxies across a wide range of Hubble types

How does the bulge Sérsic index n vary as a function of Hubble type, and galaxy stellar mass (Fig. 2.15), as well as B/T (Fig. 2.14)? The results are summarized in Table 2.9. Only a small fraction ($\sim 1\%$) of bright spirals have high $n \geq 4$ bulges; such bulges lie primarily in S0/a to Sab, and have a large $B/T > 0.2$. A moderate fraction ($\sim 22\%$) have intermediate $2 < n < 4$ bulges; these exist in barred and unbarred S0/a to Sd, and their B/T spans a wide range (0.03–0.5) with a mean of 0.29. A strikingly large fraction ($\sim 76\%$) of bright spirals have low $n \leq 2$ bulges; such bulges exist in barred and unbarred galaxies across a wide range of Hubble types, and their B/T varies from 0.01 to 0.4, with most having $B/T \leq 0.2$.

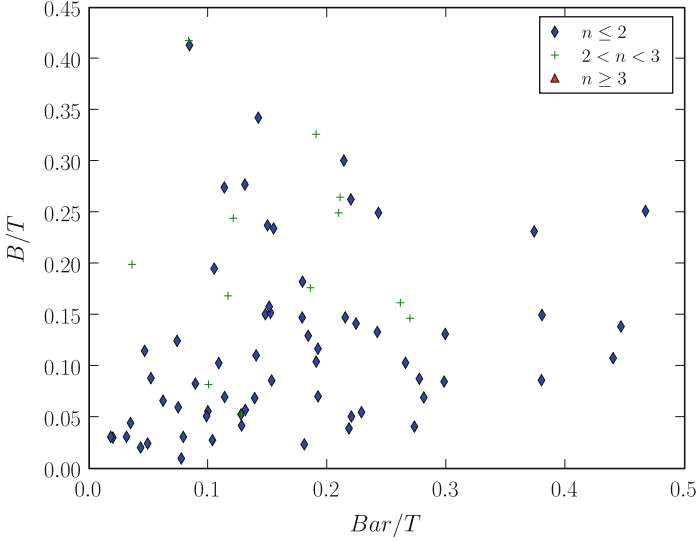


Fig. 2.16 B/T is plotted against Bar/T and sorted by bulge Sérsic index. There are six galaxies with $Bar/T \geq 0.3$

Table 2.9 B/T and bulge n in bright/high mass spirals

Sample ($M_B \leq -19.3$)	
Fraction of spirals with bulge $n \geq 4$	$1.40 \pm 0.98 \%$
Fraction of spirals with bulge $2 < n < 4$	$22.4 \pm 3.49 \%$
Fraction of spirals with bulge $n \leq 2$	$76.2 \pm 3.56 \%$
Fraction of spirals with bulge $n > 2$	$23.8 \pm 3.56 \%$
Fraction of spirals with $B/T \leq 0.2$	$68.5 \pm 3.88 \%$
Fraction of spirals with $B/T > 0.2$	$31.1 \pm 3.88 \%$
Fraction of spirals with $0.2 < B/T < 0.4$	$23.1 \pm 3.52 \%$
Fraction of spirals with $B/T \geq 0.4$	$8.39 \pm 2.32 \%$
Sample $M_* \geq 1 \times 10^{10} M_\odot$	
Fraction of spirals with bulge $n \geq 4$	$1.77 \pm 1.24 \%$
Fraction of spirals with bulge $2 < n < 4$	$23.9 \pm 4.01 \%$
Fraction of spirals with bulge $n \leq 2$	$74.3 \pm 4.11 \%$
Fraction of spirals with bulge $n > 2$	$25.7 \pm 4.11 \%$
Fraction of spirals with $B/T \leq 0.2$	$66.4 \pm 4.44 \%$
Fraction of spirals with $B/T > 0.2$	$33.6 \pm 4.44 \%$
Fraction of spirals with $0.2 < B/T < 0.4$	$25.7 \pm 4.11 \%$
Fraction of spirals with $B/T \geq 0.4$	$7.96 \pm 2.55 \%$

2.5.4 Comparison with Other Work

As an independent check of our decomposition method, we compare our results with independently published decompositions.

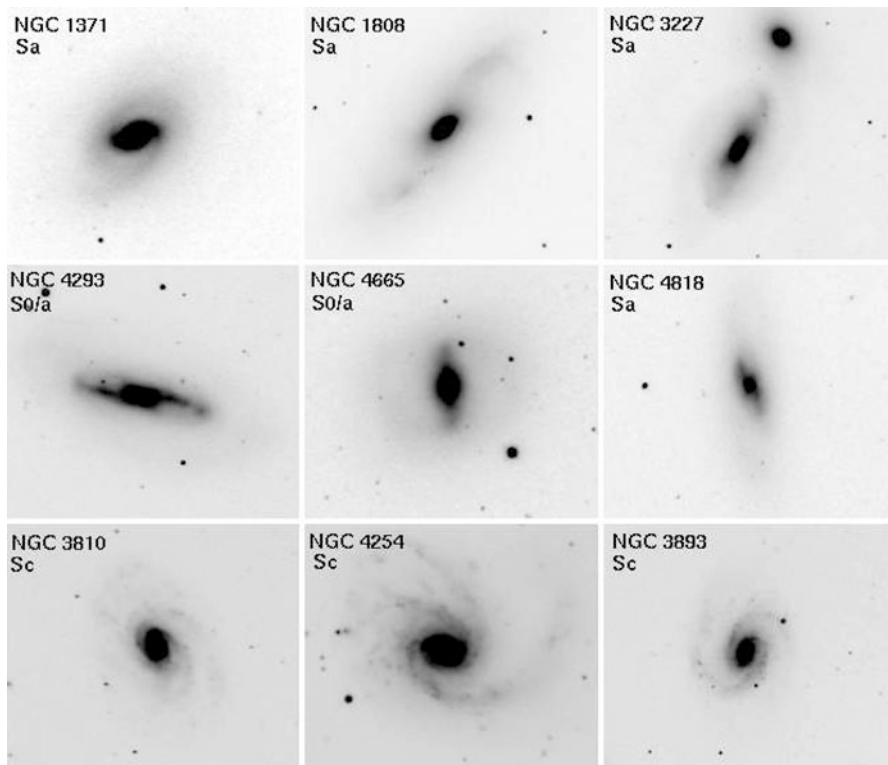


Fig. 2.17 The *top two rows* show H -band images of barred galaxies, which have early RC3 Hubble types, but yet have $B/T \leq 0.2$. The *bottom row* shows H -band images of unbarred galaxies, which have late RC3 Hubble types, but yet have $B/T \sim 0.4$. The Hubble types assigned to these objects more reflect disk smoothness and spiral arm topology than B/T . All images are from OSUBSGS with characteristics as described in Sect. 2.2

We find our mean H -band B/D (Fig. 2.18) ratios are comparable to the K -band B/D derived with the 1D bulge-disk decompositions of Graham (2001) and Trujillo et al. (2002). Like Graham (2001) and Trujillo et al. (2002), we find B/D is widely variable with Hubble type and that mean B/D steadily declines from Sa through Scd galaxies. Graham (2001) and Trujillo et al. (2002) find bulge indices are widely variable within a Hubble type, but they are in general >1 for early types and <1 for late types. We likewise find wide scatter in bulge index with $n < 1$ bulges existing in both early and late types. Figure 2.18 is also in good agreement with the more recent results of Graham and Worley (2008), who have calculated, as a function of morphology, inclination and dust-corrected B/D and bulge Sérsic indices. They find B/D values are typically $< 1/3$.

Another meaningful comparison can be made with Laurikainen et al. (2007) who, using their own 2D decomposition code, fit a hybrid sample containing some OSUBSGS galaxies combined with additional S0 galaxies. One difference between

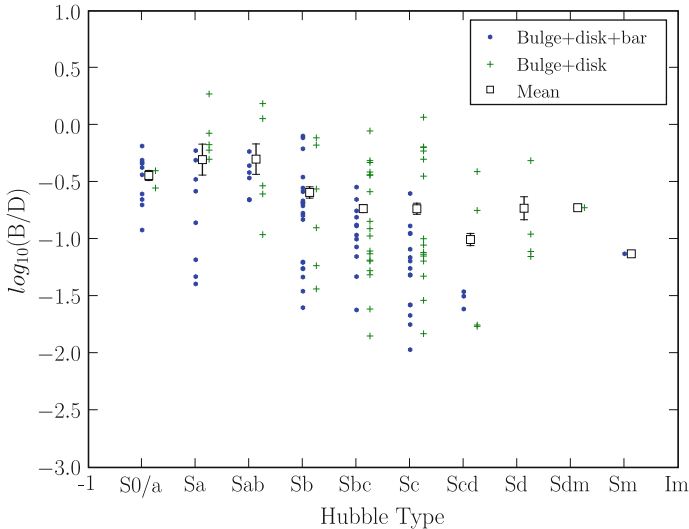


Fig. 2.18 B/D is plotted against Hubble type. The legend indicates the type of decomposition used for each data point. The mean values for barred and unbarred together in each bin are shown

their work and ours is that they typically model bars with a Ferrers function, but may sometimes use a Sérsic profile, while we use only the latter. Also, they include additional components to model secondary bars or inner disks. They report a distinct offset in the mean B/T between barred and unbarred galaxies, which we confirm in Fig. 2.15. Their mean B/T are similar to ours, and they conclude that pseudobulges exist throughout the Hubble sequence. The Sérsic indices derived by Laurikainen et al. (2007) are likewise similar, on the mean, to ours for both barred and unbarred systems. They likewise find $n \leq 2$ bulges across early and late Hubble type galaxies.

Balcells et al. (2003) emphasized that bulges typically have indices ~ 3 or lower. Our results in Fig. 2.15 are consistent. We find a low frequency ($\sim 1\%$) of high $n \geq 4$ bulges, with most bulges having $n \leq 3$.

2.5.5 Bar Strength

Stellar bars exert gravitational torques on the gaseous component and are particularly efficient in driving gas from the outer disk into the inner kiloparsec (see Sect. 2.1). Thus, it would be natural to have a measure of bar strength that is sensitive to the strength of the gravitational torque and hence measures both the shape and mass of the bar.

Many measures of bar strength have been formulated. The Q_b method of (Block et al. 2002; Buta et al. 2003, 2005) measures directly the gravitational torque at a single point along the bar. This method requires a value of scaleheight for the

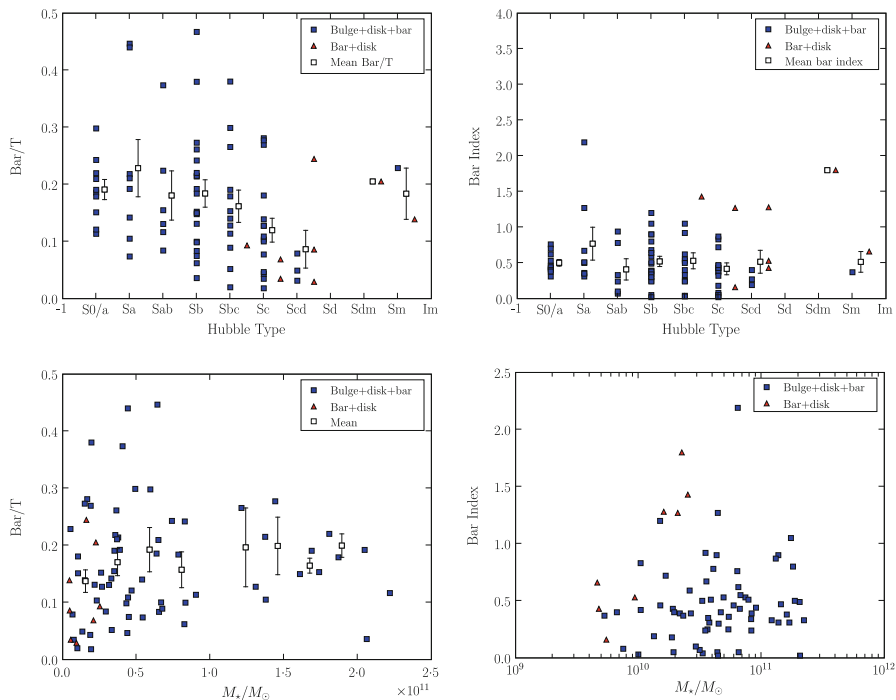


Fig. 2.19 The properties of bars are shown. The error bars indicate the standard deviation of the population around the mean in each bin. The legend in each panel indicates the type of decomposition used for each data point. *Upper left*: Mean and individual Bar/T plotted against Hubble type. *Upper right*: Mean and individual bar Sérsic indices plotted against Hubble type. *Lower left*: Bar/T plotted against total galaxy stellar mass. The mean Bar/T in bins of stellar mass is indicated. *Lower right*: Bar Sérsic index plotted against total galaxy stellar mass

disk and a model of the potential to be made from the image. In the bar/inter-bar contrast method of Elmegreen and Elmegreen (1985) and Elmegreen et al. (1996), bar strength is parameterized as the ratio between peak surface brightness in the bar region and the minimum surface brightness in the inter-bar region. Elmegreen and Elmegreen (1985) and Elmegreen et al. (1996) also characterize bar strength with the maximum amplitude of the $m = 2$ mode from Fourier decomposition. When ellipse fitting is applied, the maximum ellipticity of the bar, e_{bar} , can be used to characterize bar strength (e.g., MJ07). This constitutes a partial measure of bar strength only, however, as it offers no information about mass of the bar.

Bulge-disk-bar decomposition in the H -band provides another *partial* measure of bar strength through the H -band Bar/T light ratio, which is a measure of the Bar/T mass ratio under the assumption that the H -band M/L ratio is the same for the bar and the rest of the galaxy, as discussed in Sect. 2.5.2. Figures 2.19 and 2.20 explore the derived bar properties.

The upper left panel of Fig. 2.19 plots the individual and mean Bar/T against Hubble type. There is a wide range (~ 0.03 to ~ 0.47) in the individual Bar/T at a

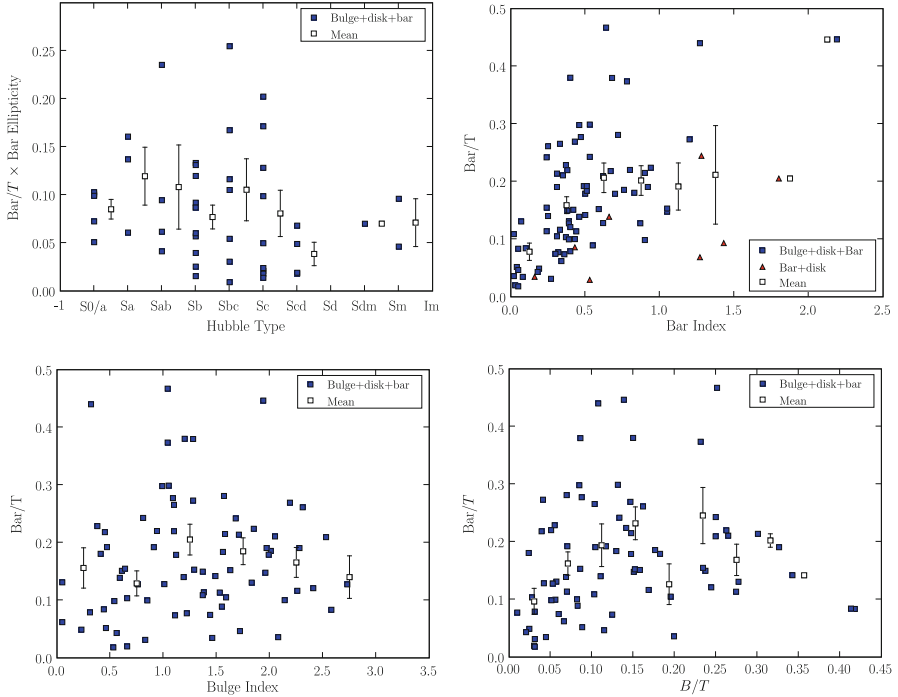


Fig. 2.20 Bar strength is plotted against Hubble type and the properties of bars are compared with bulges. The legend in each panel indicates the type of decomposition used for each data point. *Upper left:* Bar strength, the product of Bar/T and peak bar ellipticity e_{bar} from MJ07 is plotted against Hubble type. *Upper right:* Bar/T is plotted against bar Sérsic index. *Lower left:* Bar/T is plotted against bulge Sérsic index. *Lower right:* Bar/T is plotted against B/T . In the first plot, mean bar strength is calculated for each Hubble type. In the latter three plots, mean Bar/T is calculated for bins along the ordinate axis. The error bars indicate the standard deviation of the population around the mean in each bin

given Hubble type. The mean Bar/T remains fairly constant with Hubble type from Sa to Sb, but shows a possible weak decline by about 0.1 from Sb to Sc. Their number statistics are too small to make any robust statement for later Hubble types. We also note that six systems have high Bar/T above 0.3; these are displayed in Fig. 2.21.

Bar Sérsic indices are mostly below unity. Neither the individual, nor the mean bar Sérsic index, show any trend with Hubble type or with stellar mass, for Sa to Sc galaxies (Fig. 2.19). Thus, the steepness of the bar profile does not seem to depend on the Hubble type. Is the bar mass ratio and its mass profile related? There is a wide range in the individual Bar/T at a given bar Sérsic index (Fig. 2.20). The mean Bar/T rises with bar index out to a bar index of ~ 0.6 , and then flattens out. This suggests that on the mean, bars of lower Bar/T have flatter profiles.

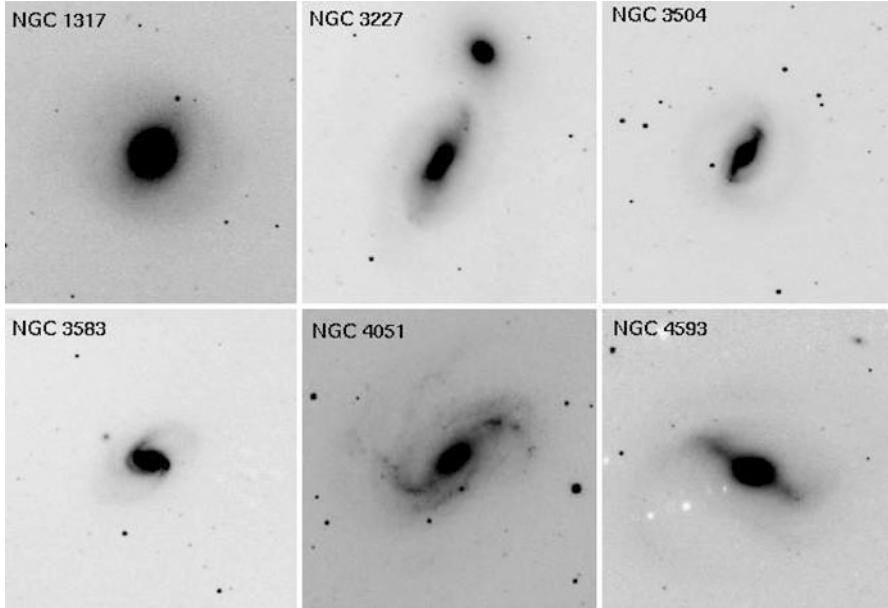


Fig. 2.21 *H*-band OSUBSGS images of spirals with prominent bars of $\text{Bar}/T > 0.3$ are shown. An interesting example is the oval or lens galaxy NGC 1317: the bar has a low ellipticity, but its B/T is large because it is extended and massive. Such bars/lenses may exert significant gravitational torques although they are not very elongated

Is there a relation between the bar strength and the bulge present in a galaxy? There is a wide range in the individual Bar/T at a given B/T , and at a given bulge Sérsic index (Fig. 2.20). The mean Bar/T shows a weak decline for bulge Sérsic indices above two. Similarly the mean Bar/T shows a weak rise from 0.1 to 0.25 as B/T rises out to 0.15, after which the trend flattens or reverses.

Both Bar/T and maximum bar ellipticity e_{bar} are partial measures of bar strength. Fig. 2.19 shows mean Bar/T may scale weakly with Hubble type. The bars with highest e_{bar} (i.e. thin bars) are often termed strong bars, and e_{bar} has been shown to correlate with Q_b . Total bar strength should scale with both bar mass and bar ellipticity. Does bar strength have a dependence on Hubble type? The upper left panel of Fig. 2.20 plots the product of Bar/T and e_{bar} , as determined by MJ07 for galaxies mutually classified as barred, against Hubble type. There is a wide range in $\text{Bar}/T \times e_{\text{bar}}$ in each bin, and mean bar strength shows no definite trend with Hubble type. We note that bars with high Bar/T and high e_{bar} should exert the largest gravitational torque and be most effective at driving gas inflows. A nice example is the oval or lens galaxy NGC 1317 (Fig. 2.21); the bar has a low ellipticity, but its B/T is large as it is extended and massive. Such bars or lenses may exert significant gravitational torques although they are not very elongated.

2.5.6 Bar Fraction as a Function of B/T and Bulge Index

As outlined in Sect. 2.5.3, we found that as many as $\sim 76\%$ of bright spirals have bulges with $n \leq 2$; such bulges exist in barred and unbarred galaxies across a wide range of Hubble types, and their spread in B/T is from 0.01 to 0.4, with most having $B/T \leq 0.2$. The variation of the bar fraction as a function of B/T and bulge n can provide important constraints on bulge formation scenarios (Sect. 2.5.8). Table 2.10 shows our results. The bar fraction declines with bulge index; $\sim 65\%$ of the spirals with low $n \leq 2$ bulges host bars while intermediate $2 < n < 4$ bulges have a lower bar fraction ($\sim 38\%$). The high $n \geq 4$ bulges in the sample are unbarred, so the bar fraction is 0%. Systems with low B/T are more likely to be barred. For $B/T \leq 0.2$, the bar fraction is high ($\sim 68\%$). Systems with $0.2 < B/T < 0.4$ and $B/T \geq 0.4$ have lower bar fraction ($\sim 42\%$ and $\sim 17\%$).

Overall, Table 2.10 shows bulges with low $n \leq 2$ and low $B/T \leq 0.2$ preferentially exist in barred galaxies. This is consistent with earlier work (Odehahn 1996; Barazza et al. 2008; Marinova et al. 2009; Aguerri et al. 2009) where an enhanced optical bar fraction is seen in galaxies with late Hubble types or low B/D . It may be tempting to infer this result to mean the formation pathway of two-thirds of low- B/T bulges is related to bars in that spontaneous or/and tidally induced bars play a role in bulge formation (with the remaining one-third of such bulges may have been formed either by mechanisms like retrograde minor mergers or short-lived bars). We caution that this type of cause-effect relationship is not the only scenario consistent with this result. It may also be possible that bar instabilities are favored in galaxies with low B/T and no inner Lindblad resonances (ILR). Under these conditions, the swing amplifier model with a feedback loop (Julian and Toomre 1966; Toomre 1981; Binney and Tremaine 1998) may be responsible for bar formation and partly account for the high bar fraction in galaxies of low B/T .

2.5.7 Formation of Bulges

Our observational results provide some interesting challenges for models of galaxy evolution that try to address the origin of present-day bulges. Any successful model must be able to account for the observed distribution of bulge B/T and n in high mass ($M_\star \geq 1.0 \times 10^{10} M_\odot$) spirals, as shown in Tables 2.9 and 2.10. In particular, the following results must be reproduced:

1. In terms of the overall distribution of bulge n , as much as ($\sim 74\%$) of high mass spirals have bulge $n \leq 2$: such bulges exist in barred and unbarred galaxies and their B/T ranges from 0.01 to 0.4, with most having $B/T \leq 0.2$ (Table 2.9). A moderate fraction ($\sim 24\%$) of high mass spirals have $2 < n < 4$, and just ($\sim 2\%$) have $n \geq 4$.
2. Theoretical models often make more robust predictions on the bulge-to-total mass ratio B/T than on the bulge index n , so we consider the empirical B/T

Table 2.10 Bar fraction as a function of B/T and bulge index

Sample ($M_B \leq -19.3$)	
Bar fraction in spirals with bulge $n \geq 4$	$0.00 \pm 0.00\%$
Bar fraction in spirals with bulge $2 < n < 4$	$37.5 \pm 8.56\%$
Bar fraction in spirals with bulge $n \leq 2$	$65.1 \pm 4.56\%$
Bar fraction of spirals with bulge $n > 2$	$35.3 \pm 8.20\%$
Bar fraction of spirals with $B/T \leq 0.2$	$68.4 \pm 4.70\%$
Bar fraction of spirals with $B/T > 0.2$	$35.6 \pm 7.14\%$
Bar fraction of spirals with $0.2 < B/T < 0.4$	$42.4 \pm 8.60\%$
Bar fraction of spirals with $B/T \geq 0.4$	$16.7 \pm 10.8\%$
Sample $M_* \geq 1 \times 10^{10} M_\odot$	
Bar fraction of spirals with bulge $n \geq 4$	$0.00 \pm 0.00\%$
Bar fraction of spirals with bulge $2 < n < 4$	$44.4 \pm 9.56\%$
Bar fraction of spirals with bulge $n \leq 2$	$63.1 \pm 5.27\%$
Bar fraction of spirals with bulge $n > 2$	$41.4 \pm 9.15\%$
Bar fraction of spirals with $B/T \leq 0.2$	$68.0 \pm 5.39\%$
Bar fraction of spirals with $B/T > 0.2$	$36.8 \pm 7.83\%$
Bar fraction of spirals with $0.2 < B/T < 0.4$	$41.4 \pm 9.15\%$
Bar fraction of spirals with $B/T \geq 0.4$	$22.2 \pm 13.9\%$

distribution in detail. We note that as much as $\sim 66\%$ of high mass spirals have bulges with $B/T \leq 0.2$ (Table 2.9). In terms of bar fraction, $\sim 68\%$ are barred (Table 2.10).

3. The fraction of bars rises among spirals with low bulge index n . About 63% of spirals with low $n \leq 2$ bulges host bars, while the bar fraction in spirals with $2 < n < 4$ bulges (44%) is two-thirds as large (Table 2.10).

In a hierarchical Universe, there are several physical processes that contribute to the assembly of bulges: major mergers, minor mergers, and secular evolution. We briefly describe these, expanding on our introduction in Sect. 2.1.

Major mergers, defined as those with mass ratio $M_1/M_2 \geq 1/4$, typically destroy the extended outer stellar disks during violent relaxation, leaving behind a classical bulge. Such bulges are associated with modest-to-high bulge Sérsic indices, in the range $2 < n < 6$ (Hopkins et al. 2009a; Springel et al. 2005; Robertson et al. 2006; Sect. 2.5.8) in simulations. This trend is also consistent with the fact that among ellipticals, high luminosity ones tend to have a Sérsic index $n > 4$, while low luminosity ones tend to have $2 \leq n \leq 3.5$ (Caon et al. 1993; Kormendy and Fisher 2008). The final Sérsic index depends on the amount of residual gas the settles into a somewhat disk component. Simulations by Hopkins et al. (2009a) find that the Sérsic indices of remnants from 1:1 gas-rich major mergers lie in the range of $2 < n < 4$, with most above 2.5 (see Fig. 2.22). This body of evidence strongly suggests that many bulges with $n > 2$ might have a major merger origin.

Minor mergers, typically defined as those with mass ratio $1/10 < M_1/M_2 < 1/4$, do not destroy the stellar disk of the primary system, but can contribute to building bulges via three pathways. Firstly, a fraction F_{sat} of the satellite's stellar mass can end up in the central region of the primary galaxy. The value of F_{sat} depends on

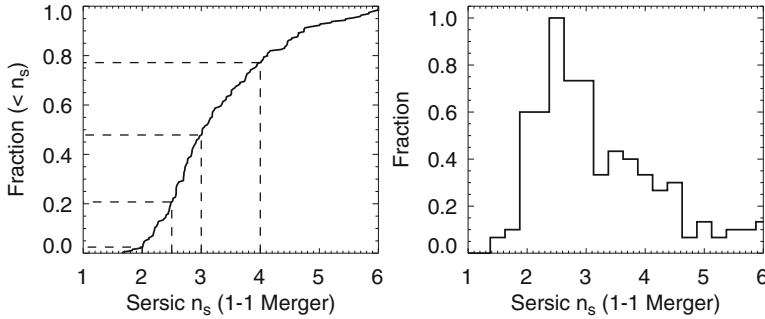


Fig. 2.22 Shown is the distribution of Sérsic indices n for remnants of 1:1 gas-rich major mergers in the simulations of Hopkins et al. (2009a): they lie in the range of $2 < n < 6$. Specifically, $\sim 22\%$ of the remnants have classical $n \geq 4$, as much as 20% have low $n \leq 2.5$, while 50% have $n \leq 3$. Almost none have $n \leq 2$. [Figure: courtesy of Phil Hopkins]

how centrally concentrated the in-falling satellite is. Typically, the more diffuse outer stellar body is tidally stripped, while the central core sinks by dynamical friction to the central region (e.g., Quinn et al. 1993; Walker et al. 1996). Secondly, a non-axisymmetric feature (e.g., a stellar bar or bar-like feature) can be induced in the main disk, and gravitational torques exerted by the feature can drive gas into the inner kpc (e.g., Hernquist and Mihos 1995; Jogee 2006 and references therein), where subsequent SF forms a compact high v/σ stellar component, or disk pseudobulge. Most of the gas inflow happens during the merger phase and large gas inflow rates (e.g., $\gg 1 M_\odot$ per year) may be generated. Thirdly, gas inflow can also be caused by direct tidal torques from the companion (e.g., Hernquist and Mihos 1995; Eliche-Moral et al. 2006). It is to be noted that in the simulations by Hernquist and Mihos (1995), the gas inflow generated by non-axisymmetric features (e.g., bar-like features) in the inner part of the disk is much larger than that caused by direct tidal torques from the satellite. In the recent work of Eliche-Moral et al. (2006), N-body simulations of minor mergers followed by fits of 1D Sérsic+exponential models to the remnants, suggest that the bulge Sérsic index and B/D ratio can grow as a result of the central re-concentration of stellar disk material in the primary system by tidal forces. Minor mergers are frequent under Λ CDM, and the likelihood of multiple successive minor mergers occurring during the formation of a galaxy is high. Bournaud et al. (2007) study the effects of repeated minor mergers on galaxy structure. They show that a disk galaxy undergoing successive minor mergers will eventually transform into an elliptical galaxy with an $r^{1/4}$ -law profile and high V/σ . However, galaxy growth is not completely merger-driven and the efficiency of minor mergers at creating ellipticals must be regulated by other mechanisms (e.g., cold gas accretion).

In addition, the process of secular evolution can build a disk bulge (pseudobulge) between merger events. Here a stellar bar or globally oval structure in a *non-interacting* galaxy drives gas inflow into the inner kpc, where subsequent star

formation forms a compact high v/σ stellar component (e.g., Kormendy 1993; Jogee et al. 1999; KK04; Jogee et al. 2005; Athanassoula 2005; Kormendy and Fisher 2005; Kormendy 2008). This process is different from that of minor mergers in the sense that it happens in the quiescent phase of the galaxy, between minor or major merger events. The prevalence of pseudobulges in galaxies of different Hubble types is discussed in KK04, and select examples of S0 galaxies with pseudobulges are also shown in Kormendy and Cornell (2004) and KK04.

The present-day bulge mass can be written as the sum of mass contributed from each process:

$$M_{bulge} = M_{bulge} \times (f_{maj} + f_{min1} + f_{min2} + f_{min3} + f_{sec}), \quad (2.6)$$

where

- f_{maj} is the percentage of the bulge stellar mass, which is built by major mergers,
- f_{min1} is the percentage of the bulge stellar mass, which is built during minor mergers from stars of the satellite. This depends on the fraction F_{sat} of the satellite's stellar mass, which ends up in the central region of the primary galaxy during each minor merger.
- f_{min2} is the percentage of the bulge stellar mass, which is built during minor mergers from gas inflow caused by a tidally induced bar.
- f_{min3} is the percentage of the stellar mass, which is built during minor mergers from gas inflow caused by tidal torques from the companion.
- f_{sec} is the percentage of the stellar mass, which is built secularly between merger events from gas inflow caused by bars or ovals

In Sect. 2.5.8, we compare our derived distribution of bulge n and B/T with hierarchical models that model major and minor mergers, but not secular evolution. The main goal of the model is to see whether bulges built via major mergers can account for the large fraction of high mass spirals with bulges of low B/T or/and low n . A secondary goal is to see if a first order simplified prescription for minor mergers can broadly account for the observations. We stress here that bulge-building during minor mergers is modeled in a very simple way: all the stars in the satellite are assumed to contribute to the bulge of the larger galaxy (i.e., $F_{sat} = 100\%$), and bulge-building via gas inflow driven through tidal torques and via gravitational torques from induced bars are ignored (i.e., $f_{min2} = 0$, and $f_{min3} = 0$). Furthermore, the models entirely ignore secular evolution between mergers. In a future paper, these extra terms will be addressed and a comprehensive picture built of the relative importance of minor mergers and secular processes in making present-day bulges.

2.5.8 Comparison of B/T with Hierarchical Models of Galaxy Evolution

We compare our data with the predictions from cosmological semi-analytical models based on Khochfar and Burkert (2005) and Khochfar and Silk (2006). We briefly describe the models first. The merger trees of dark matter (DM) halos are derived by using the extended Press–Schechter formalism (Press and Schechter 1974), as in Somerville and Kolatt (1999). When two DM halos merge, the merger time scale of the galaxies is calculated by considering the timescale it would take the satellite galaxies to reach the central galaxy at the center of the halo via dynamical friction (e.g., Kauffmann et al. 1999; Springel et al. 2001). The baryonic physics, which includes radiative cooling, star formation, and feedback from supernovae, is treated via semi-analytic prescriptions (see Khochfar and Silk 2006 and references therein). Baryonic mass inside the dark matter halos is divided between hot gas, cold gas, and stars. The hot gas is initially shock-heated to the halo virial temperature. As the gas radiatively cools, it settles down into a rotationally supported disk at the halo center. Cold disk gas is allowed to fragment and subsequently form stars according to the Schmidt–Kennicutt law (Kennicutt 1998). Star formation is regulated by feedback from supernovae using the prescription in Kauffmann et al. (1999).

Major mergers are typically considered as those with stellar mass ratio $M_1/M_2 \geq 1/4$. In the simulations, one assumes that during a major merger any existing stellar disk is destroyed, gas is converted to stars with some star formation efficiency (SFE), and all stars present undergo violent relaxation to form a bulge. Therefore, the bulge-to-total stellar mass ratio (B/T) of a bulge immediately after a major merger is always one. Note that the SFE during a major merger is not assumed to be 100% as there is mounting evidence from SPH simulations (Springel and Hernquist 2005; Cox et al. 2008) that not all cold gas is converted to stars. Instead, the burst efficiency defined by Cox et al. (2008) is applied to control the fraction of stars formed due to the interaction. This efficiency is dependent on the relative masses of merging galaxies and is expressed as

$$e = e_{1:1} \left(\frac{M_{\text{Satellite}}}{M_{\text{Primary}}} \right)^\gamma, \quad (2.7)$$

where $e_{1:1}$ is the burst efficiency for a 1:1 merger and γ fixes the dependence on mass ratio; Cox et al. (2008) find $e_{1:1} = 0.55$ and $\gamma = 0.69$. The remaining fraction $(1-e)$ of gas is added to the gaseous disk and can start making stars.

As stated above, immediately after a major merger, the remnant is a bulge with a B/T equal to one. As time proceeds, B/T falls because a stellar disk grows around the bulge as hot gas in the halo cools, settles into a disk, and forms stars. The formation of stars by any residual cold gas left at the end of the major merger also helps to grow the disk. Thus B/T falls until the next major merger happens, at which point B/T is reset to one in the models.

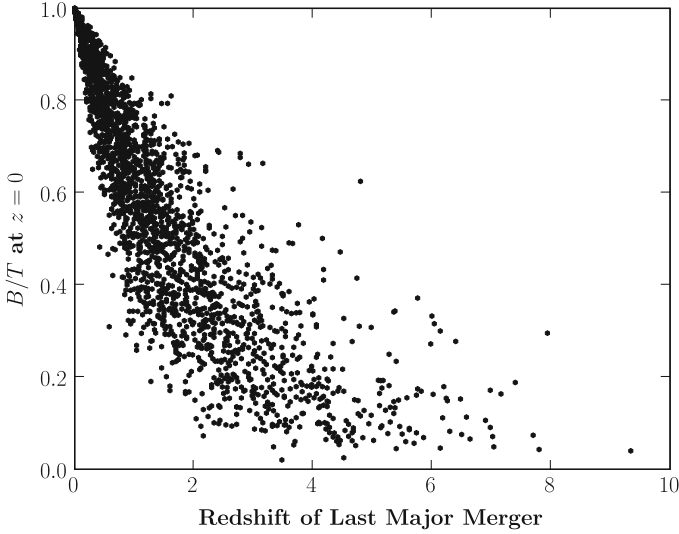


Fig. 2.23 For those high mass ($M_* \geq 1.0 \times 10^{10} M_\odot$) galaxies in the theoretical models that experienced a major merger (see Sect. 2.5.8), the B/T of the remnant at $z \sim 0$ is plotted against the redshift z_{last} of the last major merger. Systems where the last major merger occurred at earlier times have had more time to grow a disk and thus have a lower B/T at $z \sim 0$. The dispersion in the present-day B/T at a given z_{last} is due to the different times spent by a galaxy in terms of being a satellite versus a central galaxy in a DM halo, since the cooling of gas and the growth of a disk is stopped when a galaxy becomes a satellite. In the model, a high mass galaxy that has undergone a major merger at $z \leq 2$ has a present-day $B/T > 0.2$. In effect, a high mass spiral can have a present-day $B/T \leq 0.2$ only if its last major merger occurred at $z > 2$ (lookback times > 10 Gyr).

The bulge may also grow in stellar mass due to minor mergers. Minor mergers are defined as mergers with mass ratio $1/10 < M_1/M_2 < 1/4$, and the stellar disk of the large companion is not destroyed during such mergers. The models assume that during minor mergers, all the stars in the satellite are added to the bulge of the host, while the gas settles in the disk. When DM halos grow by accretion or minor mergers, the hot gas that comes in with a satellite is immediately stripped and added to the hot gas component of the host. The cold gas in the disk of the satellite is only added to the cold gas of the host if they merge. Until they merge the satellite is using up its own cold gas to make stars.

Figure 2.23 shows the relationship between the present-day B/T of a high mass ($M_* \geq 1.0 \times 10^{10} M_\odot$) spiral and the redshift z_{last} of its last major merger. As expected, systems where the last major merger occurred at earlier times, have had more time to grow a disk and have a lower B/T . The dispersion in the present-day B/T at a given z_{last} is due to the different times spent by a galaxy in terms of being a satellite versus a central galaxy in a DM halo, since the cooling of gas and the growth of a disk is stopped when a galaxy becomes a satellite. Thus, galaxies

that became a satellite galaxy shortly after their last major merger stayed at high B/T . Conversely, galaxies that continued to be a central galaxy for a long time after their last major merger will have low B/T .

The present-day B/T of a high mass ($M_{\star} \geq 1.0 \times 10^{10} M_{\odot}$) spiral depends on its major merger history. In particular, we note from Fig. 2.23 that a high mass ($M_{\star} \geq 1.0 \times 10^{10} M_{\odot}$) galaxy, which has undergone a past major merger since $z \leq 2$ will end up hosting a present-day $B/T > 0.2$. In effect, *a high mass spiral can have a present-day $B/T \leq 0.2$ only if its last major merger occurred at $z > 2$ (lookback times > 10 Gyr).*

The predicted distribution of present-day B/T depends on the galaxy merger history in the models and it is relevant to ask how well the latter is constrained observationally. Over the redshift range $z \sim 0.24$ to 0.80 (lookback times of 3–7 Gyr), recent studies by Jogee et al. (2009) find that among high mass ($M_{\star} \geq 2.5 \times 10^{10} M_{\odot}$) galaxies, $\sim 10\%$ of galaxies are undergoing mergers of mass ratio $> 1/10$, and $\sim 3\%$ are undergoing major mergers of mass ratio $> 1/4$. These findings agree within a factor of less than ~ 2 with the merger rates from the models of Khochfar and Burkert (2001) over $z \sim 0.24$ to 0.80. At higher redshifts, the empirical merger rate/fraction is uncertain due to relatively modest volumes and bandpass shifting effects, but there is a general trend towards higher merger fractions at higher redshifts (e.g., Conselice et al. 2003). The models used here (Khochfar and Burkert 2001) agree with this trend and predict that $\sim 13.5\%$ and $\sim 20\%$ of high mass ($M_{\star} \geq 1.0 \times 10^{10} M_{\odot}$) spirals have undergone major mergers since $z \leq 2$ and $z \leq 4$, respectively (see Table 2.11).

The contribution of galaxies with different merger histories to the present-day B/T distribution are shown in Table 2.11. The top and middle parts of the table describe systems with and without major mergers since $z \leq 2$ and $z \leq 4$, respectively. In the model, $\sim 13.5\%$ of present-day high mass ($M_{\star} \geq 1.0 \times 10^{10} M_{\odot}$) spirals, experienced a major merger since $z \leq 2$, causing most of them ($\sim 11.2\%$) to have a present-day high $B/T > 0.4$ and a negligible fraction ($\sim 0.1\%$) to have a low present-day $B/T \leq 0.2$. In contrast, the remaining $\sim 86.5\%$ spirals experienced no major merger at $z \leq 2$, and most (67.2%) of them have a present-day low $B/T \leq 0.2$. If the comparisons are extended to systems without a major merger since $z \leq 4$, the numbers are very similar (see middle part of Table 2.11).

Table 2.11 shows that there is good agreement between the model and data for the fraction of high mass spirals with present-day low $B/T \leq 0.2$ ($\sim 67\%$ in the model versus $\sim 66\%$ in the data). The model contribution to low $B/T \leq 0.2$ comes almost entirely from galaxies, which have not had a major merger since $z \leq 2$ (see column 4 in Table 2.11). In fact, most of these galaxies have not even had a major merger since $z \leq 4$, as illustrated by the bottom part of Table 2.11. *In the model, the fraction ($\sim 1.6\%$; column 3 of Table 2.11) of high mass spirals, which have undergone a major merger since $z \leq 4$ and host a bulge with a present-day $B/T \leq 0.2$, is a factor of over thirty smaller than the observed fraction ($\sim 66\%$) of high mass spirals with $B/T \leq 0.2$. Thus, bulges built via major mergers since $z \leq 4$ seriously fail to account for the bulges present in $\sim 66\%$ of high mass spirals. These results are also illustrated in Fig. 2.24, which shows the comparison between*



<http://www.springer.com/978-3-319-06958-6>

Probing Galaxy Evolution by Unveiling the Structure of
Massive Galaxies Across Cosmic Time and in Diverse
Environments

Weinzirl, T.

2015, XIV, 236 p. 73 illus., 43 illus. in color., Hardcover

ISBN: 978-3-319-06958-6